

A DETAILED ANALYSIS OF THE HIGH RESOLUTION X-RAY SPECTRA OF NGC 3516: VARIABILITY OF THE IONIZED ABSORBERS

E. M. Huerta^{1,2}, Y. Krongold¹, F. Nicastro³, S. Mathur⁴, A. L. Longinotti⁵ & E. Jimenez-Bailon¹.

ABSTRACT

The 1.5 Seyfert galaxy NGC 3516 presents a strong time variability in X-rays. We re-analyzed the 9 observations performed on October 2006 by XMM-Newton and Chandra in the 0.3 to 10 keV energy band. An acceptable model was found to the XMM-Newton data fitting EPIC-PN and RGS spectra simultaneously; later, this model was successfully applied to the contemporary Chandra high resolution data. The model consists of a continuum emission component (power law + blackbody) absorbed by four ionized components (warm absorbers), and ten narrow emission lines. Three absorbing components are warm, producing features only in the soft X-ray band. The fourth ionization component produces FeXXV and FeXXVI in the hard-energy band. We study the time response of the absorbing components to the well detect changes in the X-ray luminosity of this source, and find that the two components with the lower ionization state show clear opacity changes consistent with gas close to photoionization equilibrium. These changes are supported by the models and by differences in the spectral features among the nine observations. On the other hand, the two components with higher ionization state do not seem to respond to continuum variations. The response time of the ionized absorbers allows us to constrain their electron density and location. We find that one component (with intermediate ionization) must be located within the obscuring torus, at a distance 2.7×10^{17} cm from the central engine. This outflowing component is likely originated in the accretion disk. The three remaining components are at distances larger than 10^{16-17} cm. Two of the absorbing components in the soft X-rays have similar outflow velocities and locations. These components may be in pressure equilibrium, forming a multi-phase medium, if the gas has metallicity larger than the solar one ($Z \gtrsim 5Z_{\odot}$). We also search for variations in the covering factor of the ionized absorbers (although partial covering is not required in our models). We find no correlation between the change in covering factor and the flux of the source. This, in connection with the observed variability of the ionized absorbers, suggests that the changes in flux are not produced by this material. If the variations are indeed produced by obscuring clumps of gas, these must be located much closer in to the central source.

Subject headings: X-rays: galaxies, Galaxies: active, Galaxies: nuclei, Galaxies: Seyfert.

¹Departamento de Astronomía Extragaláctica y Cosmología, Instituto de Astronomía, Universidad Nacional Autónoma de México (UNAM), Apartado Postal 70-264, 04510, México DF, México.

²Departamento de Física, Universidad Autónoma Metropolitana Iztapalapa (UAM-I), Av. San Rafael Atlixco 186, 09340, México, D.F. México.

³Osservatorio Astronomico di Roma-INAF, Via di Fras-

cati 33, 00040, Monte Porzio Catone, RM, Italy.

⁴Astronomy Department, The Ohio State University, Enarson Hall, 140 W. 18th Avenue, Columbus, OH 43210, USA.

⁵European Space Astronomy Centre of ESA, Madrid, Spain

1. Introduction

In $\sim 50\%$ type 1 Active Galactic Nuclei (AGN) (e.g. George et al. (1998); Piconcelli et al. (2005)) absorption lines are detected in the far UV and the soft X-ray spectral ranges (Mathur et al. 1995, 1997). These lines, which are blue-shifted, are generated by several ionized species. Nearly one hundred features are produced in these media with outflow velocities of the order of few hundred to thousand kms^{-1} (Crenshaw et al. 2003; Krongold et al. 2003). The location of this absorbing material, referred to as the warm absorber (WA) (Halpern 1984) remains uncertain. Suggestions range from the accretion disk itself (Elvis 2000; Krongold et al. 2005a, 2007, 2010; Longinotti et al. 2013) to the obscuring torus (Blustin et al. 2005) and the narrow-line region (e.g. Ricci et al. (2010)). There are several models that attempt to explain the distribution and physical conditions of the absorbing gas. One of them proposes that different WA phases can coexist in pressure equilibrium, a multiphase medium (Krongold et al. 2003, 2005b; Cardaci et al. 2009). Another one suggests that the material, also in pressure equilibrium, is distributed with a radial stratification (Rózańska et al. 2006). Most X-ray analysis have been based on photoionization models (e.g. Netzer et al. (2003); McKernan et al. (2007); Andrade-Velázquez et al. (2010); Longinotti et al. (2010)), where the properties of the absorbing gas are described in terms of the Hydrogen equivalent column density and its ionization state. These studies have yielded WA multiphase winds with equivalent column density values $N_H \sim 10^{21-23} \text{ cm}^{-2}$. In this kind of models, the ionization state of the WA components is characterized by the ionization parameter (here defined as $U = \frac{Q}{4\pi R^2 n_H c}$, where Q is the rate of 0.013-100 keV photons produced in the source, R the distance between the black hole and the accretion disk system to WA location, n_H the Hydrogen number density and c the light speed). As noted by Nicastro et al. (1999) and Krongold et al. (2007) there is a degeneracy in this formula, as only the product $n_e R^2$ can be inferred from observables. However, time variability analysis solve this problem: by measuring the response time of the absorber to variations in the impinging continuum, the density n_H can be estimated (Nicastro et al. 1999) and therefore the distance from the source to the ionized absorber

can be constrained (see also Krolik & Kriss (1995); Reynolds et al. (1995); Krongold et al. (2007, 2010)).

Studying the properties of the absorbing material is of great importance, as it has been suggested that these outflows can play an important role in galaxy evolution. If the outflowing material is a significant fraction of the accreted mass they can provide the feedback proposed by the cosmological models (Di Matteo et al. 2005; Hopkins et al. 2006)).

1.1. Seyfert 1.5 galaxy NGC 3516

NGC 3516 is a Seyfert 1.5 galaxy (Véron-Cetty & Véron 2006) at $z = 0.00886$ (Keel 1996) that presents an extreme X-ray flux variability (Edelson et al. 2000; Netzer et al. 2002; Turner et al. 2008; Markowitz et al. 2008). NGC 3516 is also extremely variable in optical and UV emission (see as examples: Voit et al. (1987); Walter et al. (1990); Crenshaw et al. (1998); Goad et al. (1999); Edelson & Nandra (1999); Maoz et al. (2002); Kraemer et al. (2002)).

The source has been observed in X-rays from 1979 (Maccacaro et al. 1987) to 2009 (Turner et al. 2011) with all the X-ray observatories (Kolman et al. 1993; Nandra & Pounds 1994; Morse et al. 1995; Kriss et al. 1996; Edelson & Nandra 1999; Costantini et al. 2000; Guainazzi et al. 2001; George et al. 2002; Turner et al. 2008, 2011). NGC 3516 presents a complex spectrum: in the soft X-ray range (0.3 - 2 keV), the spectrum shows the so-called *Soft Excess*, several absorption features attributed to the presence of warm absorbers and few emission lines (Costantini et al. 2000; Guainazzi et al. 2001; George et al. 2002; Turner et al. 2005, 2008; Mehdipour et al. 2010). In the hard band (2 to 200 keV), it presents the fluorescence Iron emission line $K\alpha$ and two absorption lines by FeXXV and FeXXVI. To fit the hard band X-ray continuum of this source Turner et al. (2005) fitted a Power Law, finding a Photon Index $\Gamma \sim 2$ in the 10 - 200 keV regime. Also Markowitz et al. (2008) fitted an absorbed Power Law with $\Gamma = 2$ over the 0.3 - 76 keV range. Recently, Mehdipour et al. (2010) reported a significant change in the slope of the Power Law among 2006 XMM-Newton observations: Γ varied from 1.70 ± 0.2 to 1.85 ± 0.2 , in addition to significant changes in the 0.2 to 10 keV range flux.

To model the Soft Excess emission Markowitz et al. (2008) added a second Power Law, with the same Photon Index as the primary power law but not obscured by any absorber. Mehdipour et al. (2010) added a modified Black Body component which describes the spectrum of a Black Body reprocessed by coherent Compton scattering. The best fit temperature varied from 186 ± 3 eV to 211 ± 4 eV. We note that the Soft Excess physical interpretation is still an issue (see Ricci et al. (2010)).

1.2. Previous analysis of the Ionized Absorber in NGC 3516

The complex absorption in NGC 3516 soft X-ray band was detected by two strong absorption features at 0.74 and 0.87 keV with *ROSAT* (Mathur et al. 1997) and *ASCA* X-ray telescopes (Kriss et al. 1996). These features were originally interpreted as absorbing K edges due to OVII and OVIII bound-free transitions. More recently, a few high ionization absorption components producing both absorption lines and edges have been detected in high resolution spectra. Turner et al. (2005) reported three ionization states: (1) a “cool” absorber with a column density $N_H \sim 6 \times 10^{21} \text{ cm}^{-2}$ and an outflow velocity $v_{out} = 200 \text{ km s}^{-1}$ (all the outflow velocities in this work were fixed to a given value), associated with the “UV absorber” found by Kraemer et al. (2002); (2) a “high ionization” absorber with $N_H \sim 10^{22} \text{ cm}^{-2}$ and a fixed $v_{out} = 1100 \text{ km s}^{-1}$; and (3) a “heavy” absorber with $N_H \sim 10^{23} \text{ cm}^{-2}$ and $v_{out} = 1100 \text{ km s}^{-1}$, that covers only 50% of the continuum source. Later on, Turner et al. (2008) discovered a fourth absorbing component, with even higher ionization state, through the positive detection of H-like and He-like features of Fe XXV and XXVI. This component, only detectable in the hard X-ray band, has $N_H \sim 10^{23} \text{ cm}^{-2}$ and $v_{out} \sim 1000 \text{ km s}^{-1}$. Turner et al. (2008) interpreted the flux variations in the X-ray band as the result of variations in the covering fraction of the “heavy absorber”.

Using low resolution *Suzaku* data, Markowitz et al. (2006) found two absorbing components: A “primary absorber” with properties consistent with the “heavy” absorber reported by Turner et al. (2008) (although with a covering fraction of 96–100%) and a mildly-ionized medium, consistent

with the “UV absorber”. Mehdipour et al. (2010) analyzed the XMM Newton data of the source. They detected the same three absorbing components as Turner et al. (2008), but they reported that partial covering is not required by the data for the heavy absorber. If these authors impose a partial absorber in their models, they further find that variations in the covering fraction are not consistent with the data (in contrast to the results by Turner et al. (2008)).

Finally, Holczer & Behar (2012) found a kinematic structure in the absorber, consisting in four different outflow components intrinsic to NGC 3516: (1) $v_{out} = -350 \pm 100 \text{ km s}^{-1}$, (2) $v_{out} = -1500 \pm 150 \text{ km s}^{-1}$, (3) $v_{out} = -2600 \pm 200 \text{ km s}^{-1}$, and (4) $v_{out} = -4000 \pm 400 \text{ km s}^{-1}$. Holczer & Behar (2012) analyzed the Chandra high resolution spectra obtained in 2001 and 2006. They detect variability in this structure, noting that the high velocity components are only present in the 2006 observations. They further report that the covering factor plays a minor role in the absorption lines.

In the UV band Kraemer et al. (2002) have reported eight different kinematic absorbing components. Using data obtained by the *GHR*S (Goddard High Resolution Spectrograph) on board the Hubble Space Telescope (*HST*), these authors detected four of these components through Ly α , CIV, and NV absorption lines with radial velocities of -376, -183 and -36 km s^{-1} (where the last system is comprized by a blend of two different kinematic components). Later on, the other four kinematic components were detected with the Space Telescope Imaging Spectrograph (*STIS*) on board the HST. These components present radial velocities of -692, -837, -994, and -1372 km s^{-1} . These authors suggest that the emergence of the new components is the result of variations of ionized gas in response to changes in the ionizing continuum.

1.3. X-ray Variability on NGC 3516

As it has been reported NGC 3516 presents strong flux variations in time, from the optical-UV to the X-rays (see for example Koratkar et al. (1996) and Kraemer et al. (2002)). The source presents extreme X-ray flux variations, by a factor of 5 on timescales of hours (Turner et al. 2008), and by a factor of 50 in timescales of years (Netzer et al. 2002). These variations are often associated

with spectral changes (e.g. Netzer et al. (2002); Turner et al. (2008) and references therein) not only in the energy flux, there is evidence of spectral features variability (Mathur et al. 1997; Netzer et al. 2002; Turner et al. 2008; Holczer & Behar 2012). To understand the nature of the variability, some scenarios invoking obscuration have been proposed: Costantini et al. (2000) suggested neutral clouds that hide the central source (using *Beppo SAX* telescope spectra), Markowitz et al. (2008) (with *Suzaku* spectra) proposed a model in which flux variations could be explained by the presence of discrete blobs or filaments located within few light years of the black hole, traversing the line of sight during the observation time. Turner et al. (2008) suggested a simple explanation were that only parameter varying among observations (and producing both the flux and spectral variations) is the covering factor of the heavy absorber phase.

Other interpretations suggest that rather, the variations might be intrinsic to the source. Mehdipour et al. (2010) arrived to this conclusion using 2006 XMM Newton spectra.

However, in a most recent X-ray NGC 3516 analysis, using *Suzaku* 2009 X-ray observations, Turner et al. (2011) claims an absence of reverberation signals. This led them to conclude that intrinsic continuum variability is not possible. They suggested that the variability can be a consequence of Compton-thick clumps of gas in the line-of-sight.

In this paper we present the analysis of all 2006 X-ray observations available in the XMM-Newton Science Archive (*XSA*) and Chandra Data Archive (*CDA*) of NGC 3516. We study the both high and low resolution spectra to cover the range between 0.3 keV to 10 keV. We first present the analysis over individual spectra to characterize the spectral components, and then study the time variability of the absorber among observations. In our analysis we find variations in two of the ionized absorbers in response to continuum variations.

Section §2 describes the X-ray observations and the data reduction. In section §3, we present 2006 X-ray data analysis and the best model for XMM data, we also describe the Chandra analysis. Section §4 contains our results, including the time variability behaviour and a physical scenario proposed to explain the X-ray properties and the flux

variability of NGC 3516. We discuss our results in section 5. Finally in section 6 we present the conclusions.

2. X-ray Observations and Data Reduction

X-ray observations of NGC 3516 were obtained with XMM-Newton (Jansen et al. 2001) and Chandra X-ray Observatory (Weisskopf et al. 2000) in October 2006. The log of observations is presented in Tables 1 and 2, for XMM-Newton and Chandra X-ray observatories respectively. In the following we describe the data properties and reduction process.

2.1. XMM-Newton Observatory Data

We studied all the NGC 3516 XMM-Newton X-ray spectra from the *RGS* (Reflection Grating Spectrometer) and the *EPIC-PN* (European Photon Imaging Camera). The observations were performed between October 6 to October 12 of 2006.

The RGS data were processed with the standard pipeline of Science Analysis System (*SAS*) v8.0.1 (Gabriel et al. 2004). We produced source and background spectra, as well as response matrices for the RGS data with the *rgsproc* task. The RGS spectra were grouped into two channels per bin. We considered the wavelength range from 8 to 38 Å [0.33 - 1.55 keV], that covers most of the soft X-ray band.

EPIC-PN spectra were also generated using *SAS*. First, intervals of flaring particle background were selected in order to clean the event list using the method presented in Piconcelli et al. (2004). The spectra were extracted from a circle with center on the observed position of NGC 3516 and radius $\sim 40''$ in all observations. The background spectra were obtained from a circular region with similar radius in the same chip of the source. No sign of pile-up was detected in any of the observations as reported before by Turner et al. (2008) and Mehdipour et al. (2010). The source and background spectra were generated with the *evselect* task. Then, the redistribution matrix and the ancillary files were created with the *rmfgen* and the *arfgen* tasks, respectively. The spectra were grouped to a minimum of 20 counts per bin in order to be able to use χ^2 statistics. We selected the interval from 0.3 keV to 10 keV that includes the

TABLE 1
OBSERVATIONS MEAN COUNT RATE AND EXPOSURE TIME OF XMM-NEWTON OBSERVATIONS TAKEN IN
OCTOBER OF 2006

Observation	ObsID	Obs. Date [Year/Month/Day]	Exposure time [seconds]			Mean Count Rate [counts/sec] $\pm \sigma$		
			PN	RGS	RGS	PN	RGS	RGS
1 XMM [1x]	0401210401	2006-10-06	36142	51558		30.80	0.90	
2 XMM [2x]	0401210501	2006-10-08	48031	68752		28.60	0.84	
3 XMM [5x]	0401210601	2006-10-10	47534	68203		15.61	0.49	
4 XMM [8x]	0401211001	2006-10-12	47608	67813		27.45	0.96	

TABLE 2
OBSERVATIONS COUNT RATE AND EXPOSURE TIME OF CHANDRA OBSERVATIONS TAKEN IN OCTOBER OF
2006

Observation	ObsID	Obs. Date [Year/Month/Day]	Exposure time [seconds]			Mean Count Rate [counts/sec] $\pm \sigma$	
			MEG	HEG	HEG	MEG	HEG
1 CXO [3c]	8452	2006-10-09	19832	19832	0.62	0.32	
2 CXO [4c]	7282	2006-10-10	41410	41410	0.41	0.23	
3 CXO [6c]	8451	2006-10-11	47360	47360	0.74	0.38	
4 CXO [7c]	8450	2006-10-12	38505	38505	0.79	0.39	
5 CXO [9c]	7281	2006-10-14	42443	42443	0.40	0.23	

soft and hard X-ray bands. In Table 1 the net count rate and the exposure time for each obsID and detector of the XMM-Newton observations of NGC 3516 are shown.

2.2. Chandra X-ray Observatory Data

The Chandra X-ray observations were performed from October 9 to October 14 in 2006 using the High Energy Transmission Grating (*HETGS*) with the *ACIS-S* (Advanced CCD Imaging Spectrometer). The *HETGS* (Canizares et al. 2000) contains two grating assemblies, the Medium Energy Grating (*MEG*) and High Energy Grating (*HEG*). We extracted spectra from both gratings using the Chandra Interactive Analysis of Observations software (*CIAO v.3.4*, Fruscione et al. (2006)) (we followed the standard pipeline processes). Negative and positive first-order spectra, and their response matrices were obtained and co-added. The spectra were grouped into two channels per bin. The count rates and the exposure time in the Medium Energy Grating and High Energy Grating spectra are given in Table 2.

3. Data Analysis

3.1. Time Variability

The 2006 X-ray observations of NGC 3516 were performed with almost continuous time coverage (with XMM-Newton and/or Chandra) in a time scale of nine days (see Tables 1 and 2). We have numbered the observations in sequential order according to the date of observation, and further included a **x** suffix if performed by XMM-Newton or a **c** suffix if obtained with Chandra.

There is strong flux variability among different observations with the same observatory (compare count rates for observations with the same observatory/instrument in Tables 1 and 2) and within single observations. A detailed light curve of the nine observations can be observed in Figures 1 and 2 of Turner et al. (2008). In this paper, we study the temporal evolution of the absorbing components in response to these flux changes.

3.2. XMM-Newton Spectral Analysis

We performed the analysis of the XMM-Newton observations using simultaneously both the EPIC-PN and RGS data sets. All spectra were analyzed

with the *Sherpa* (Freeman et al. 2001) package included in the CIAO software. Throughout the paper, we attenuate all models with an equivalent H column density $N_H = 3.23 \times 10^{20} \text{ cm}^{-2}$ (Dickey & Lockman 1990) to account for the Galactic Absorption in the line of sight towards NGC 3516.

3.2.1. Analysis in the X-ray Hard Energy Band

First, we modelled the NGC 3516 EPIC-PN spectra in the 2.5 - 10 keV band. We fit the data using a redshifted Power Law model plus a Gaussian to account for the Fe-K α emission line reported by Turner et al. (2008) and Mehdipour et al. (2010). This model presents strong negative residuals around 7 keV, confirming the two significant absorption lines reported by Turner et al. (2008) and Mehdipour et al. (2010), corresponding to Fe K transitions of FeXXV and FeXXVI. These features were modelled with Gaussians at this initial stage (although a self consistent photoionization model was applied to this absorption system later on). Table 3 lists the best fit parameters for each observation. The model is statistically acceptable for all observations (Table 3).

3.2.2. X-ray Broad Band Analysis

We fit the EPIC-PN and RGS simultaneously, extrapolating the fit in the hard band to the entire spectrum [0.3 - 10 keV]. A soft X-ray excess is evident in the residuals. We fit this emission feature with a Black Body. Initially, we left the temperature of the Black Body free to vary independently among observations. However, since in all XMM-Newton observations the kT value is always around 0.1 keV (see Table 4), this parameter was free to vary but constrained to have the same value in all observations (the temperature of the Black Body was linked to a single best fit value among the all observations). The normalization was fit independently in each observation.

This model presents strong residuals in the soft band typical of ionized absorption, due to the well known warm absorber in this source.

3.2.3. Modelling the Ionized Absorber in NGC 3516

There have been several studies of the warm absorbers in NGC 3516, reporting a different number of ionization components. In order to establish the

TABLE 3
HARD BAND FIT: 2.5 - 10 KEV ENERGY BAND.

Obs	Power law		Fe-K α	FeXXV	FeXXVI	Statistics χ_{red}/dof [2.5 - 10 keV]
	Γ	Norm ^a	Pos[keV] σ [keV] Norm ^b	Pos[keV] σ [keV] Norm ^b	Pos[keV] σ [keV] Norm ^b	
1x	1.64 ± 0.02	1.22 ± 0.02	$6.38^{+0.03}_{-0.02}$ $0.13^{+0.05}_{-0.03}$ $5.89^{+0.64}_{-0.84}$	6.73 ± 0.03 0.04 ± 0.04 $-1.42^{+0.31}_{-0.30}$	7.04 ± 0.02 0.05 ± 0.04 -1.58 ± 0.03	0.79/1364
2x	1.59 ± 0.02	0.99 ± 0.02	6.39 ± 0.02 0.12 ± 0.02 $7.37^{+0.43}_{-0.45}$	6.703 ± 0.019 0.03 ± 0.04 -1.15 ± 0.23	7.05 ± 0.02 0.05 ± 0.04 -1.38 ± 0.23	1.08/1411
5x	1.45 ± 0.02	0.65 ± 0.02	6.38 ± 0.02 0.13 ± 0.02 $7.29^{+0.44}_{-0.45}$	6.75 ± 0.02 0.02 ± 0.04 -1.06 ± 0.21	7.08 ± 0.02 0.03 ± 0.03 -1.16 ± 0.22	1.17/1357
8x	1.54 ± 0.02	0.95 ± 0.02	6.41 ± 0.02 0.09 ± 0.02 $5.89^{+0.48}_{-0.47}$	6.78 ± 0.02 0.04 ± 0.03 -1.84 ± 0.31	$7.11^{+0.03}_{-0.02}$ 0.05 ± 0.03 -1.86 ± 0.32	0.79/1483

^ain 10^{-2} photons/keV/cm²/s at 1 keV

^bin 10^{-5} photons/cm²/s in the line

TABLE 4
WHOLE BAND FIT: 0.3 - 10 KEV.

Obs	Power law	Black Body	Statistics χ_{red}/dof [0.3,10 keV]
	Γ Norm ^a	kT [keV] Norm ^c	
1x	1.31 ± 0.02 0.78 ± 0.02	0.08 ± 0.02 5.92 ± 0.05	4.5/4534
2x	1.30 ± 0.02 0.66 ± 0.02	0.09 ± 0.02 5.85 ± 0.04	5.2/4581
5x	1.05 ± 0.02 0.36 ± 0.02	0.09 ± 0.02 2.99 ± 0.03	4.2/4527
8x	1.21 ± 0.02 0.61 ± 0.02	0.09 ± 0.02 6.38 ± 0.04	5.2/4655

^ain 10^{-2} photons/keV/cm²/s in al 1 keV

^cin 10^{-4} L_{39}/D_{10}^2 units, L_{39} is the source luminosity in units of 10^{39} ergs/sec and D_{10} is the distance to the source in units of 10 kpc

presence of each component, we decided to add one absorber component at a time in our models. This allows us to test statistically its presence, and also to inspect visually its contribution to the overall opacity.

The *PHASE* code (Krongold et al. 2003) was used to fit the warm absorbers (WA). The model has four free parameters: 1) The ionization parameter U ($U = \frac{Q}{4\pi R^2 n_H c}$)¹; 2) the equivalent Hydrogen column density N_H ; 3) the outflow velocity v_z ; and 4) the internal micro-turbulence velocity v_{turb} . The spectral energy distribution (*SED*) of the source, also required in the models, was obtained from *NED* (NASA/IPAC Extragalactic Database) between the radio and the UV regimes, and complemented with our fits to the X-ray band. The SED is shown in Figure 1.

We note that the estimated errors in the outflow velocity of the absorber are too small, in general, smaller than the resolution of the detectors. For this reason, throughout the paper we consider a conservative error in this parameter as half the minimum spectral resolution of the RGS (700 kms^{-1} in 15 Å): $\Delta v_{out} = 350 \text{ km s}^{-1}$. We prefer this conservative value given that the fits to the data include several blended absorption lines from different charge states as well as the blend of several velocity components present in absorption.

Our first model (**Model A**) consists of a single ionization component, and an F-test confirms its presence with $> 99.99\%$ confidence level for all observations. This component models absorbing lines produced mainly by OVII, OVIII, as well as part of the Fe M-shell unresolved transition array (*UTA*), among others. The outflow velocity is $-532 \pm 350 \text{ kms}^{-1}$.

Model B included a second WA absorbing phase. A statistically better fit than **Model A** is supported by an F-test ($> 99.99\%$ of significance for all XMM-Newton observations). The second absorber fits absorption lines with higher level of ionization, mainly Fe L-shell absorption from charge states XVII to XXII, also including absorption by NeX. The outflow velocity is higher

also, $-1845 \pm 350 \text{ kms}^{-1}$. We note that the two ionized absorption phases had different U and N_H values among observations. We will analyze these changes in section 4.1.

Given that residuals were still present, we further included a third WA phase (**Model C**). At the beginning, all the parameters were free to vary. However, for each absorbing component, the best-fit value of the outflow velocity v_{out} among the observations was similar, with differences lower than the RGS resolution: 700 kms^{-1} (in 15 Å). Thus, we left the outflow velocity of each absorber as a free parameter, but constrained it to have the same best-fit value in all the observations (we link this parameter in the models for all observations, assuming no acceleration or deceleration in the flow during the total observing time). Given that the best fit values of the turbulent velocity v_{turb} were also very similar among observations, with differences lower than RGS resolution, we performed the same procedure with the turbulent velocity, linking this free parameter to a single value in all datasets. According to an F-test, the third absorber included in model C is statistically required by the data (probability $> 99.99\%$). This third absorber is modelling low ionization lines produced by charge states such as NeV, and NeVI, and a fraction of the Fe M-shell UTA. This component had an outflow velocity best-fit value higher than the other two absorbers, $v_{out} = -2425 \pm 350 \text{ kms}^{-1}$.

Thus, this final model includes of 3 absorbing components. The first one consists of a medium level of ionization (hereafter phase **MI**); the second phase presents high ionization (hereafter phase **HI**) and the third one is produced by low ionized gas (hereafter phase **LI**). Tables 5 and 6 summarize the models applied in the four XMM-Newton spectra.

Although the data does not present strong residuals consistent with additional absorption features, we tested a possible fourth WA component in the soft X-ray RGS data. An F-test does not show a statistic improvement over Model C.

3.2.4. Emission Features in the Spectra

The presence of positive residuals in the spectra, associated to emission lines in the rest

¹Ionization parameter: $U = \frac{Q}{4\pi R^2 n_H c}$, where Q is the rate of 0.013-100 keV photons produced in the source, R the distance between the black hole and the accretion disk system to WA location, n_H the Hydrogen number density and c the light speed.

TABLE 5
MODELS TO FIT NGC 3516 IN XMM-NEWTON OBSERVATIONS

Model	Power Law		Black Body		WA parameters			Statistics	
	Γ	Norm ^a	KT	Norm ^c	Phase LI	Phase MI	Phase HI	χ_{red}/dof	
Obs 1x									
A	1.69 ± 0.02	1.36 ± 0.02	0.10 ± 0.02	9.18 ± 0.06		✓		1.44/4530	
B	1.78 ± 0.02	1.58 ± 0.04	0.10 ± 0.02	$5.29^{+0.04}_{-0.09}$		✓	✓	0.95/4526	
C	1.81 ± 0.02	1.67 ± 0.06	0.09 ± 0.02	6.47 ± 0.02	✓	✓	✓	0.86/4504	
Obs 2x									
A	1.66 ± 0.02	1.11 ± 0.02	0.10 ± 0.02	$5.82^{+0.08}_{-0.05}$		✓		1.73/4577	
B	1.71 ± 0.02	1.23 ± 0.02	0.10 ± 0.02	5.78 ± 0.04		✓	✓	1.16/4573	
C	1.74 ± 0.05	1.31 ± 0.09	0.09 ± 0.02	6.50 ± 0.40	✓	✓	✓	1.04/4557	
Obs 5x									
A	1.47 ± 0.02	0.68 ± 0.02	0.10 ± 0.02	$5.82^{+0.08}_{-0.05}$		✓		1.23/4523	
B	1.54 ± 0.02	0.79 ± 0.02	0.10 ± 0.02	$3.06^{+0.03}_{-0.05}$		✓	✓	0.98/4519	
C	1.61 ± 0.02	0.89 ± 0.02	0.09 ± 0.02	4.39 ± 0.04	✓	✓	✓	0.88/4503	
Obs 8x									
A	1.63 ± 0.02	1.13 ± 0.02	0.10 ± 0.02	8.09 ± 0.05		✓		1.74/4649	
B	1.70 ± 0.02	1.28 ± 0.02	0.09 ± 0.02	$6.23^{+0.05}_{-0.03}$		✓	✓	1.12/4645	
C	1.75 ± 0.05	1.4 ± 0.2	0.09 ± 0.02	7.9 ± 0.4	✓	✓	✓	0.97/4629	

^aIn 10^{-2} photons/keV/cm²/s in at 1 keV

^bIn 10^{-4} L_{39}/D_{10}^2 units, L_{39} is the source luminosity in units of 10^{39} ergs/sec and D_{10} is the distance to the source in units of 10 kpc

TABLE 6
WA PARAMETERS OF NGC 3516.

Model C	Phase LI		Phase MI		Phase HI	
	$\log U$ v_{el_z} [kms $^{-1}$]	$\log N_H$ $v_{el_{turb}}$ [kms $^{-1}$]	$\log U$ v_{el_z} [kms $^{-1}$]	$\log N_H$ $v_{el_{turb}}$ [kms $^{-1}$]	$\log U$ v_{el_z} [kms $^{-1}$]	$\log N_H$ $v_{el_{turb}}$ [kms $^{-1}$]
Obs 1x						
A			$0.29^{+0.03}_{-0.02}$ -888 ± 350	21.82 ± 0.02 286 ± 350		
B			0.16 ± 0.02 -995 ± 350	21.65 ± 0.02 220 ± 350	$1.65^{+0.12}_{-0.02}$ -2302 ± 350	22.07 ± 0.02 320 ± 350
C	$-0.93^{+0.03}_{-0.02}$ -2425 ± 350	21.14 ± 0.02 88 ± 350	0.38 ± 0.02 -532 ± 350	21.56 ± 0.02 239 ± 350	1.69 ± 0.02 -1845 ± 350	22.25 ± 0.02 112 ± 350
Obs 2x						
A			0.27 ± 0.02 -1018 ± 350	21.82 ± 0.02 207 ± 350		
B			0.18 ± 0.02 -1082 ± 350	21.68 ± 0.02 195 ± 350	1.95 ± 0.02 -1851 ± 350	22.29 ± 0.08 77 ± 350
C	-0.78 ± 0.05 $\Rightarrow 1x$	20.98 ± 0.08 $\Rightarrow 1x$	0.27 ± 0.02 $\Rightarrow 1x$	21.52 ± 0.09 $\Rightarrow 1x$	1.68 ± 0.09 $\Rightarrow 1x$	22.197 ± 0.164 $\Rightarrow 1x$
Obs 5x						
A			0.215 ± 0.024 -1388 ± 350	21.94 ± 0.02 168 ± 350		
B			0.12 ± 0.02 -1066 ± 350	21.75 ± 0.02 199 ± 350	1.68 ± 0.02 -885 ± 350	22.22 ± 0.03 143 ± 350
C	-1.22 ± 0.02 $\Rightarrow 1x$	21.25 ± 0.02 $\Rightarrow 1x$	0.29 ± 0.02 $\Rightarrow 1x$	21.62 ± 0.02 $\Rightarrow 1x$	1.77 ± 0.02 $\Rightarrow 1x$	22.33 ± 0.14 $\Rightarrow 1x$
Obs 8x						
A			0.33 ± 0.02 -1154 ± 350	21.93 ± 0.02 202 ± 350		
B			0.18 ± 0.03 -619 ± 350	21.69 ± 0.02 234.9 ± 350	1.77 ± 0.02 -2293 ± 350	22.07 ± 0.02 417 ± 350
C	-0.78 ± 0.02 $\Rightarrow 1x$	21.25 ± 0.09 $\Rightarrow 1x$	0.38 ± 0.02 $\Rightarrow 1x$	21.512 ± 0.032 $\Rightarrow 1x$	1.96 ± 0.22 $\Rightarrow 1x$	22.48 ± 0.22 $\Rightarrow 1x$

^ain 10^{-2} photons/keV/cm 2 /s in at 1 keV

^bin 10^{-4} L_{39}/D_{10}^2

*In model C we referred the v_{out} and v_{out} to the values of observation 1x, however the final values were fitted taking into account the four XMM-Newton observations.

TABLE 7
EMISSION LINES IN THE SOFT BAND OF XMM-NEWTON AND CHANDRA.

Transition ^a	NeIX $\lambda 13.69^*$	FeXIX $\lambda 13.91^*$	OVII $\lambda 17.39^*$	FeXIX $\lambda 17.86^*$	OVII $\lambda 21.60^*$	OVII $\lambda 21.81^*$	OVII $\lambda 22.10^*$	FeXXI $\lambda 28.53^*$	NeVI $\lambda 28.92^*$
Observation	Wavelength Observed [\AA] Energy Flux ^b								
1x	13.79 \pm 0.08 1.4 \pm 0.5	14.04 \pm 0.04 2.4 \pm 0.6	17.73 \pm 0.02 1.9 \pm 0.05	18.05 \pm 0.12 1.9 \pm 0.05	21.64 \pm 0.02 9.8 \pm 3.2	21.93 \pm 0.02 3.9 \pm ...	22.29 \pm 0.22 0.9 \pm 0.8	28.83 \pm 0.03 0.5 \pm 0.2	29.19 \pm 0.02 2.6 \pm 0.7
2x	13.79 \pm 0.02	14.04 \pm 0.02	17.67 \pm 0.03	18.19 \pm 0.03	21.59 \pm 0.02	21.89 \pm 0.08	22.29 \pm 0.09	28.86 \pm 0.02	29.18 \pm 0.02
3c	13.81 \pm 0.10 1.5 \pm 0.9	14.06 \pm 0.02 2.6 \pm 1.3	17.67 \pm ... 1.5 \pm 1.8	18.16 \pm 0.72 2.2 \pm 2.1	21.6 \pm ... 0 \pm ...	21.91 \pm ... 3.4 \pm ...	22.30 \pm ... 3.4 \pm ...	0.2 \pm 0.5 O.R. ^c	2.9 \pm 0.7 O.R.
4c	13.82 \pm 0.04 0.8 \pm 0.5	14.06 \pm 0.06 1.07 \pm 0.7	17.74 \pm 0.08 0.7 \pm 0.6	18.215 \pm 18.16 \pm ...	21.59 \pm ... 1.5 \pm ...	21.82 \pm 7.7 \pm 7.2	22.31 \pm ... 6.2 \pm 5.5	O.R.	O.R.
5x	13.79 \pm 0.02	14.04 \pm 0.02	17.65 \pm 0.02	18.16 \pm ...	21.64 \pm	21.89 \pm 0.2	22.29 \pm 0.02	28.82 \pm ...	29.19 \pm 0.04
6c	13.82 \pm 0.04 0.9 \pm 0.6	14.06 \pm 0.02 2.2 \pm 0.8	17.64 \pm ... 0.4 \pm 0.4	18.11 \pm 0.10 2.6 \pm 1.5	21.62 \pm 0.02 709 \pm 645	21.90 \pm 0.04 3.6 \pm 2.2	22.31 \pm ... 4.5 \pm 2.6	0.4 \pm 0.6 O.R.	1.2 \pm 0.5 O.R.
7c	13.81 \pm ... 0.6 \pm 0.7	14.05 \pm 0.02 1.4 \pm 0.9	17.71 \pm 0.04 2.2 \pm 1.4	18.08 \pm ... 1.02 \pm 1.33	N.D. ^e 0 \pm ...	21.92 \pm 0.36 2.2 \pm 3.2	22.26 \pm 1.2 \pm 6.2	O.R.	O.R.
8x	13.79 \pm ...	14.04 \pm	17.78 \pm 0.02	18.07 \pm 0.15	21.62 \pm 0.12	21.88 \pm	22.31 \pm 0.02	N.D.	29.21 \pm 0.08
9c	1.1 \pm 1.9 13.82 \pm 0.2 0.9 \pm 1.3	0.8 \pm 0.9 14.07 \pm 1.8 3.6 \pm 4.2	0.6 \pm 0.5 17.714 \pm 0.12 1.15 \pm 1.3	6.2 \pm 4.8 18.02 \pm 0.7 1.6 \pm 1.5	123 \pm 115 N.D. 0 \pm ...	2.4 \pm 0.6 N.D. 0 \pm ...	1.99 \pm 0.75 22.3 \pm ... 1.6 \pm ...	0 \pm ... O.R.	2.2 \pm 1.7 O.R.

^aIon Name and Transition Rest-Frame Wavelength (\AA)^{*}

^bin 10^{-4} photons/cm²/s in the line

^c... means indeterminate.

^dO.R. means line out of detector range.

^eN.D. means line not detected.



Fig. 2.— RGS spectrum of observation **1x** together with the **Model C** fit -red- [8 - 38 Å]. The absorption lines are identified above with the corresponding transition and the main emission lines are marked in blue (top on the panel). The detector gaps the cool pixels of RGS are marked in blue on the bottom of the panel (<http://heasarc.gsfc.nasa.gov/docs/xmm/uhb/rgsmultipoint.html>).



Fig. 2.— RGS spectrum of observation **1x** together with the **Model C** fit -red- [8 - 38 Å]. The absorption lines are identified above with the corresponding transition and the main emission lines are marked in blue (top on the panel). The detector gaps the cool pixels of RGS are marked in blue on the bottom of the panel (<http://heasarc.gsfc.nasa.gov/docs/xmm/uhb/rgsmultipoint.html>).

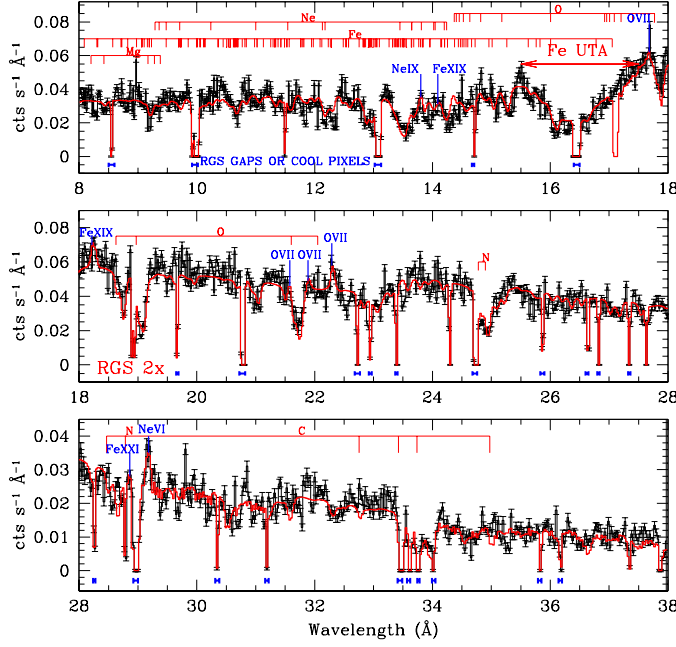


Fig. 3.— RGS spectrum of observation **2x** together with the **Model C** fit -red- [8 - 38 Å]. The absorption lines are identified above, the corresponding transition and the main emission lines are marked in blue (top on the panel). The detector gaps or the cool pixels of RGS are marked in blue on the bottom of the panel (<http://heasarc.gsfc.nasa.gov/docs/xmm/uhb rgsmultipoint.html>).

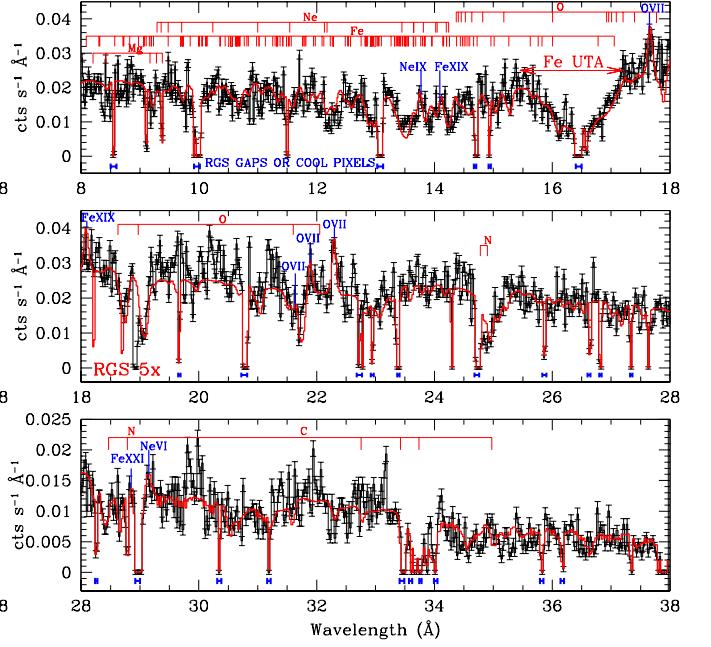


Fig. 4.— RGS spectrum of observation **5x** together with the **Model C** fit -red- [8 - 38 Å]. The absorption lines are identified above, the corresponding transition and the main emission lines are marked in blue (top on the panel). The detector gaps or the cool pixels of RGS are marked in blue on the bottom of the panel (<http://heasarc.gsfc.nasa.gov/docs/xmm/uhb rgsmultipoint.html>).

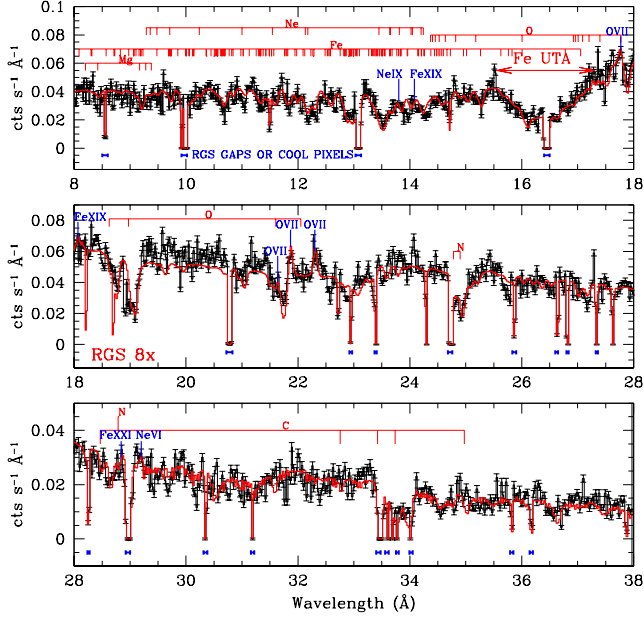


Fig. 5.— RGS spectrum of observation **8x** together with the **Model C** fit -red- [8,38 Å]. The absorption lines are identified above, the corresponding transition and the main emission lines are marked in blue (top on the panel). The detector gaps or the cool pixels of RGS are marked in blue on the bottom of the panel (http://heasarc.gsfc.nasa.gov/docs/xmm/uhb_rgsmultipoint.html).

frame of the object, is evident in the data. Through a detailed visual inspection we identified nine emission features using ATOMDB version 1.3.1 from the Chandra X-ray Center (<http://asc.harvard.edu/atomdb/WebGUIDE/>), and modelled them with Gaussian components. The Full Width at Half Maximum (*FWHM*) was fixed to 300 km s^{-1} , given that they are not resolved. We found two emission lines corresponding with Ne transitions (NeVI and NeIX), five corresponding to OVII, three of them belong to the triplet between 21.6-22.1 Å, and two lines of highly ionized Iron (FeXIX and FeXXI). Table 7 shows the nine emission lines detected in the soft X-ray band for each observation.

We stress that not all the emission lines were detected in a significant way in all the observations. However, the fluxes of all lines are consistent with each other among all the observations, with the only exception of the OVII-K α transition at λ 21.6 Å. The differences in this transition are probably due to the strong blending of this line with the strong absorption feature produced by the WA. We point out that Mehdipour et al. (2010) only modelled one emission line in the soft X-ray energy band, namely OVII (f). These authors only include this feature as it is the only one significant in all observations. Nevertheless, in their Figure 6 it is possible to observe residuals coincident with the emission lines identified here. For instance at wavelengths around $\lambda \sim 13.8$, ~ 17.8 , ~ 18 , ~ 22.2 and ~ 29.2 Å.

Summarizing, our final model consists of **Model C** (including the 3 absorbing component in the soft band) plus the fourth absorbing phase (**VH**) in the hard band, plus the nine emission lines described above. The figures with the final models (including a simultaneous fit to the Chandra and XMM data, see §3.3) are presented in Figures 2, 3, 4, 5 and 6. Table 8 contains the observed energy flux values for all observations. The flux was integrated in two different energy ranges: in the soft energy band [8 - 25 Å : 0.49 - 1.55 keV] and in the hard energy band [1.55 - 10 keV]. The reported quantities correspond to the intrinsic flux of the source, without attenuation by Galactic absorption (see §3.2) and the warm absorber components.

TABLE 8
ENERGY FLUX [$F_{h\nu}$] OF NGC 3516: SOFT X-RAY BAND AND HARD X-RAY BAND .

Obs	Soft band $F_{h\nu}^*$ [8 - 25 Å: 0.49 - 1.55 keV]	Hard band $F_{h\nu}^*$ [1.55 - 10 keV]
1x	1.87 ± 0.05	2.59 ± 0.03
2x	1.69 ± 0.03	2.34 ± 0.02
3c	1.09 ± 0.04	2.04 ± 0.03
4c	0.707 ± 0.019	1.58 ± 0.03
5x	0.88 ± 0.03	1.97 ± 0.02
6c	1.54 ± 0.03	2.22 ± 0.05
7c	1.72 ± 0.03	$2.13^{+0.08}_{-0.06}$
8x	1.84 ± 0.04	2.46 ± 0.03
9c	0.50 ± 0.02	$0.35^{+0.03}_{-0.02}$

*In $10^{-11} \text{ ergs/cm}^2/\text{s}$.

3.3. Simultaneous XMM-Newton and Chandra Spectral Analysis

Once we had a satisfactory fit with XMM-Newton, we proceeded to model the contemporary Chandra spectra. We fit the Chandra data applying a model consisting of Model C (including the three ionized absorbers detected in the soft energy band) plus the nine emission lines included in the XMM-Newton fits. Both MEG [2 - 25 Å: 0.5 - 6.2 keV] and HEG data [1.6 - 15 Å: 0.8 - 7.7 keV] were fitted simultaneously.

All nine observations (including those from XMM-Newton and Chandra) were fitted simultaneously leaving free to vary independently in each observation the Photon Index and normalization of the Power Law, and the normalization of the Black Body. The temperature kT [keV] of the Black Body emission was free to vary, but constrained to have a single value in all data. The ionization parameter and the column density of the three absorbing components was also fitted independently among different observations. However, as before, the outflow and turbulent velocities of each phase were free to vary, but linked between the nine observations to give a single best-fit value.

The best fit parameters of this final model are presented in Table 9. The fits over the high resolution (RGS) spectra are shown in Figures 2,3, 4 and 5 for observations **1x**, **2x**, **5x** and **8x** respectively. The MEG of Chandra data and best fit models are shown in Figure 6. All statistical results are satisfactory with $\chi_{red} \sim 1$ (Table 9). We note that the values for the ionization parameter

and column density on each XMM-Newton observation are consistent within 35% (and within the errors) with those found over the fits excluding the Chandra data (Model C, §3.2).

We further included in our models the fourth absorbing component (present only in the hard energy band), leaving free to vary independently among the observations the ionization parameter and column density, but constraining the outflow and turbulent velocities to a single best-fit value in all observations. Our results are summarized in Tables 9 and 10.

Finally, given that the outflow velocities of components **HI** and **LI** are similar, we tried a model with these parameters linked to a single value for both components. The warm absorber best fit parameters did not change significantly than with the Model C, §3.2. The velocity found for those two phases (phase **HI** and **LI**) is $v_{out} = -1905 \pm 350 \text{ kms}^{-1}$.

3.4. Fitting the two absorption features in the hard X-ray band of XMM-Newton and Chandra

We included in our models a fourth WA component with a very high ionization level, to fit the two absorption lines detected in the hard band (these lines were initially identified with transitions by FeXXV and FeXXVI and fitted with Gaussians over the EPIC-PN data). This fourth absorber was modelled only on the EPIC-PN data of XMM-Newton from 3 to 10 keV and the HEG (High Energy Grating) spectra of Chandra in the 3 - 7.7 keV hard X-ray band. An F-test gives us a confi-

TABLE 9
Model C ALL XMM-NEWTON AND CHANDRA OBSERVATIONS

Observation	Power Law Γ Norm ^a	Black Body kT [keV] Norm ^c	Phase HI logU logN _H v _{out} [kms ⁻¹] -1847 ± 350	Phase MI logU logN _H v _{out} [kms ⁻¹] -605 ± 350	Phase LI logU logN _H v _{out} [kms ⁻¹] -2426 ± 350	Statistics χ_{red}/dof
1x	1.82 ± 0.02 1.69 ± 0.02	0.09 ± 0.02 6.47 ^{+0.06} _{-0.09}	1.76 ± 0.02 22.33 ± 0.02 -1847 ± 13	0.42 ± 0.02 21.56 ± 0.02 -605 ± 27	-1.07 ± 0.04 21.13 ± 0.05 -2426 ± 5	0.87/4504
2x	1.77 ± 0.02 1.33 ± 0.02	6.67 ± 0.05	1.77 ± 0.02 22.27 ^{+0.04} _{-0.02}	0.36 ± 0.02 21.46 ± 0.02	-0.73 ± 0.02 21.17 ± 0.03	1.01/4558
3c	1.509 ^{+0.033} _{-0.028} 1.05 ± 0.02	6.67 ± 0.05 4.14 ± 0.06	2.14 ^{+0.08} _{-0.09} 22.37 ^{+0.09} _{-0.08}	0.28 ^{+0.17} _{-0.12} 21.408 ^{+0.119} _{-0.082}	-0.815 ^{+0.204} _{-0.132} 21.53 ^{+0.07} _{-0.08}	0.62/980
4c	1.39 ^{+0.03} _{-0.02} 0.66 ± 0.02	2.84 ± 0.04	2.05 ± 0.08 22.22 ± 0.09	0.16 ^{+0.17} _{-0.19} 21.40 ^{+0.19} _{-0.07}	-0.59 ^{+0.16} _{-0.17} 21.55 ± 0.06	0.68/980
5x	1.62 ± 0.02 0.905 ^{+0.009} _{-0.011}	4.25 ± 0.06	1.82 ^{+0.05} _{-0.08} 22.49 ± 0.12	0.27 ± 0.03 21.59 ± 0.02	-1.13 ± 0.02 21.29 ^{+0.04} _{-0.02}	0.87/4504
6c	1.58 ± 0.02 1.38 ± 0.03	5.65 ± 0.04	2.24 ± 0.03 22.44 ^{+0.04} _{-0.05}	0.65 ^{+0.015} _{-0.24} 21.67 ^{+0.03} _{-0.04}	-0.54 ± 0.17 21.45 ^{+0.03} _{-0.06}	1.08/980
7c	1.69 ± 0.02 1.58 ^{+0.05} _{-0.04}	6.13 ± 0.05	2.06 ^{+0.07} _{-0.03} 22.40 ± 0.05	0.53 ^{+0.04} _{-0.08} 21.61 ^{+0.08} _{-0.06}	-0.65 ^{+0.13} _{-0.08} 21.403 ^{+0.037} _{-0.077}	0.95/980
8x	1.75 ± 0.02 1.41 ± 0.02	5.33 ± 0.02	2.03 ± 0.02 22.52 ± 0.02	0.45 ± 0.02 21.47 ± 0.02	-0.81 ± 0.04 21.31 ± 0.02	0.95/4630
9c	1.27 ^{+0.03} _{-0.02} 0.62 ^{+0.02} _{-0.02}	2.94 ± 0.05	2.45 ^{+0.05} _{-0.12} 22.44 ^{+0.08} _{-0.09}	0.17 ± 0.15 21.57 ± 0.06	-0.83 ^{+0.22} _{-0.26} 21.54 ^{+0.06} _{-0.07}	0.74/980

^aIn 10⁻² photons/keV/cm²/s in at 1 keV.

^cIn 10⁻⁴ L₃₉/D₁₀².

^dIn 10⁻¹¹ ergs/cm²/s.

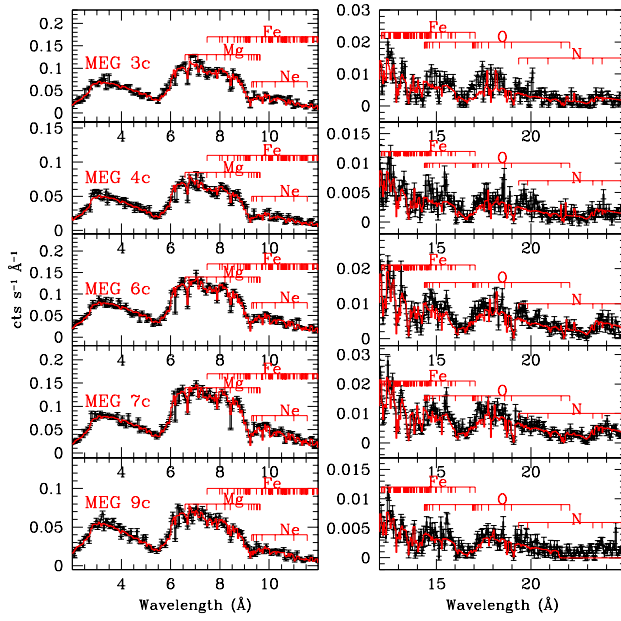


Fig. 6.— MEG spectra in $[2 - 25 \text{ \AA}]$ range of each Chandra observation together with the **Model C** fit -red-. The absorption lines are identified above with the corresponding transition -red-.

dence level larger than 99.99% for the existence of this absorber (hereafter **VH**) in all XMM-Newton observations. We found $\log U \sim 3.8$ and $\log N_H \sim 23.2$ (see Table 10). Figure 7 shows the spectra and best fit over the EPIC-PN data.

It is important to clarify that the hard X-rays were fitted separately of the soft X-ray band. However, to fix the power law in the soft energy band we took account into the hard band in the fit, with the aim to have the best fit value connected with the soft energy band. We also note that the soft absorbers have no effect on the hard energy band.

First, we fitted simultaneously three spectra of each XMM-Newton observation, RGS 1 & RGS 2 $[8 - 38 \text{ \AA}: 0.33 - 1.55 \text{ keV}]$ and EPIC-PN spectra in the energy range of $0.3 - 10 \text{ keV}$, the EPIC-PN spectra were included with the aim to obtain the best parameter of the power law. Then, we fitted the Fe-K α emission line in 6.38 keV and two absorption lines of FeXXV and XXVI in 6.7 and 6.96 keV respectively. In this model (Model C) were included 10 emission lines in the soft energy band. The model C was applied successfully into the five spectra of MEG $[2 - 25 \text{ \AA}: 0.5 - 6.2 \text{ keV}]$ and HEG spectra $[1.6 - 15 \text{ \AA}: 0.8 - 7.7 \text{ keV}]$, both Chandra high resolution detectors. Finally we cut the spectra of EPIC-PN from 3 to 10 keV and HEG spectra from $3 - 7.7 \text{ keV}$ to obtain the fourth and highest ionized absorber VH.

4. Summary of Results and Comparison with Previous Works

In order to study in detail the variability of the WA in NGC 3516, we have re-analyzed nine different individual observations from XMM-Newton and Chandra satellites. Our results show that the best fit model for all spectra consists of a variable continuum emission absorbed by three partially ionized absorbers (WA) accounting for the soft band and a fourth highly ionized WA detected only in the hard band. Tables 9 and 10 summarize the values of the parameters of this model (Model C) for each observation. As can be observed in these tables, there are significant variations in some parameters of the model among observations. In the following, we discuss the general properties of these absorbers, and defer the time resolved analysis for section 4.1.

The different ionization components produce

TABLE 10

PHASE **VH** APPLIED IN THE HARD BAND SPECTRA [3 - 10 KEV], EPIC-PN OF XMM-NEWTON AND HEG [3 - 7.7 KEV] OF CHANDRA. THE OUTFLOW VELOCITY IS GIVEN BY $v_{out} = -2650 \pm 350 \text{ kms}^{-1}$.

Obs	VH.logU	VH.logN _H	Statistics χ_{red}/dof
1x	$3.87^{+0.09}_{-0.08}$	23.22 ± 0.02	0.65/1067
2x	$3.88^{+0.08}_{-0.06}$	23.22 ± 0.02	0.81/1116
3c	$3.99 \pm \dots$	$23.26^{+0.07}_{-0.24}$	0.76/103
4c	$3.91^{+ \dots}_{-0.32}$	23.22 ± 0.06	1.25/103
5x	3.88 ± 0.42	23.23 ± 0.02	0.78/1062
6c	$4.14^{+ \dots}_{-0.06}$	$23.27^{+0.03}_{-0.59}$	1.33/103
7c	$3.51^{+ \dots}_{-0.91}$	$23.18^{+0.02}_{-0.52}$	1.01/103
8x	3.75 ± 1.08	23.22 ± 0.02	0.7/1188
9c	$3.49^{+1.27}_{-0.37}$	$23.28^{+0.27}_{-0.37}$	0.82/103

*... means indeterminate.

different absorption features. If we analyze them we found that, in the soft band, the highest ionized phase **HI** produces absorption by several Fe L-shell transitions with charge state XVIII - XXII in the 10 - 16 Å range; absorption features by SiXIII - SiXIV (between 5 and 7 Å); NeX absorption lines at 9.29, 9.36, 9.48 and 10.24 Å; and the OVIII transition at 18.97 Å. Phase **HI** electron temperature is $T_{HI,e} = 4.5 \times 10^5 \text{ K}$ and the outflow velocity is $v_{out,HI} = -1847 \pm 350 \text{ kms}^{-1}$. Phase **MI** imprints absorption features due to OVII (at 16.96, 17.01, 17.09, 17.2, 17.4, 17.77, 18.62 and 21.6 Å), OVIII (at 14.63, 14.45, 14.41, 14.82, 18.97 Å), and the most energetic portion of the Fe M-shell UTA (between 15 and 17 Å). The electron temperature associated to phase **MI** is given by $T_{MI,e} = 9.8 \times 10^4 \text{ K}$, while the outflow velocity is $v_{out,MI} = -605 \pm 350 \text{ kms}^{-1}$. Phase **LI** produces absorption lines by OVII at $\sim 16.9 - 18.6 \text{ Å}$ and the low energy part of the M-shell Fe UTA (16.5 - 18 Å). This phase also produces absorption lines by NeV - NeVI between 12 and 14 Å. It has an electron temperature $T_{LI,e} = 3.0 \times 10^4 \text{ K}$ and an outflow velocity $v_{out,LI} = -2426 \pm 350 \text{ kms}^{-1}$. Figure 8 shows the absorption features produced by each of the three absorbing phases (**HI**, **MI** and **LI**).

On other hand, the fourth hard absorption phase **VH** produces the Fe K complex in the hard band. Its electronic temperature and outflow velocity are $T_{VH} = 7.0 \times 10^5 \text{ K}$ and $v_{out,VH} = -2649 \text{ kms}^{-1}$ respectively (see Table 9).

Given that several works have analyzed the

2006 X-ray spectra of this source, a comparison among different results is mandatory. In Table 11 we present the different parameters found in the different analyses. We note that the definition of the ionization parameter used by Turner et al. (2008) and Mehdipour et al. (2010), is different than the one presented here. These authors used the ionization parameter ξ ², while our analysis was done with the parameter U ¹. Also, the Spectral Energy Distribution is different in the different analyses. Therefore, a direct comparison of the ionization parameter is not possible. However, all works are in agreement in the sense that all require three different ionized absorbers, each imprinting absorption by similar charge states in the soft X-ray energy band. The fourth highly ionized absorber (found in the hard energy band) reported by Turner et al. (2008) as **Zone 4** clearly corresponds with phase **VH** in this work.

In general, the column densities are also in agreement among the different works. The column density N_H of phase **LI** is similar to that reported by Turner et al. (2008) and Mehdipour et al. (2010). The values of N_H for components **HI** and **VH** correspond to those by Turner et al. (2008) for **Zone 3** and **Zone 4**, respectively. We note, however, that there is a significant difference in the column density of the mid-ionized absorber **MI** with respect to the **Zone 2** (Turner et

²Ionization parameter ξ : $\xi \equiv L/nr^2$ where L is 1-1000 Rydbergh luminosity, n the gas density and r the absorber-source distance.

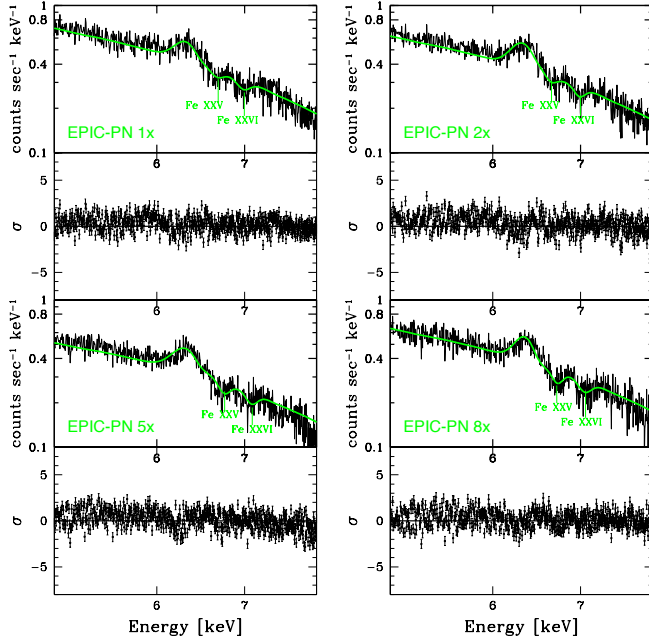


Fig. 7.— EPIC-PN spectra in [5 - 8 keV] range of each XMM-Newton observation together with the Power Law function absorbed by phase **VH** fit (in green).

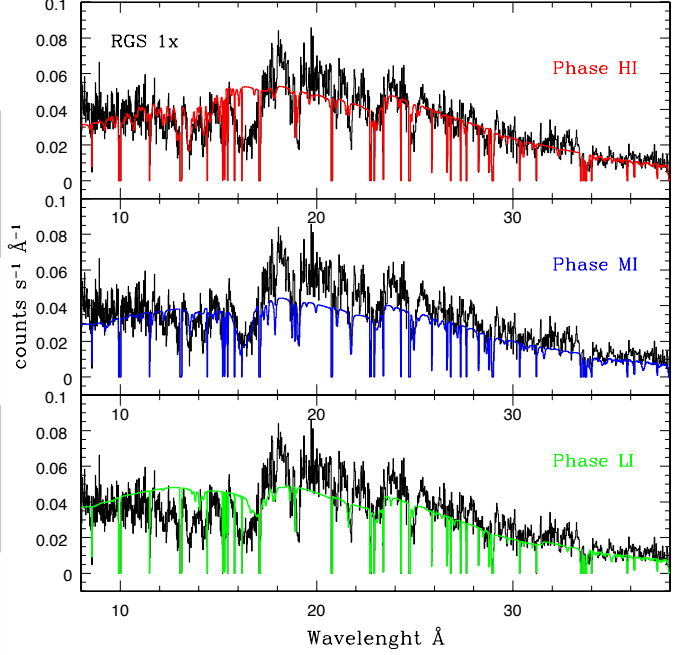


Fig. 8.— RGS spectrum of observation **1x** -black- from 8 to 38 Å. Phase **HI** (top panel) is drawn in red color, as it can be observed, it reproduces absorption lines mainly in the lowest wavelengths of the spectrum. Phase **MI** (medium panel), in blue color, reproduces the Fe M-shell UTA array and some absorption lines due to OVII and OVIII transitions. Finally, phase **LI** (bottom panel), drawn in green color, generates a fraction of the Fe-UTA and also the main absorption features around 18 Å.

al. 2008) and **Phase B** (Mehdipour et al. 2010). This change can be explained by the fact that we assumed full coverage for all absorbers in our analysis (but see §4.2.2).

The most intriguing difference in this work with respect to previous analyses is present in the different outflow velocities of the absorbers: Phases **LI**, **HI** and **VH** present outflow velocities significantly larger than previously found. Instead, phase **MI** presents a smaller outflow velocity than the components of middle ionization of these other works. It is worth to mention that in Turner et al. (2005) the velocity of their **Zone 1** was fixed to an outflow velocity of -200 km s^{-1} , but in Turner et al. (2008) a value $v_{out} \sim -1000 \text{ km s}^{-1}$ is reported for this same component. Furthermore, Turner et al. (2008) based the outflow velocities in only 11 absorption lines (see their Table 1). Overall, the differences in velocity are likely produced because the different absorption lines are present with a range of velocities, that are not fully resolved in the data.

This is further evidenced by Holczer & Behar (2012), who made a detailed analysis of the kinematic components in the high resolution spectra of Chandra: They found evidence of four kinematic components with different outflow velocities. According to these authors, the slower components (with $v_{out} = -350 \pm 100 \text{ km s}^{-1}$ and $v_{out} = -1500 \pm 150 \text{ km s}^{-1}$) present a broad range of ionization, while the two faster components ($v_{out} = -2600 \pm 200 \text{ km s}^{-1}$ and $v_{out} = -4000 \pm 400 \text{ km s}^{-1}$) are more highly ionized. Phases **MI**, **HI** and **VH** of the model proposed in this work are consistent with the results by Holczer & Behar (2012). The higher outflow velocity of component **LI** is discussed below, in section 5.2.

4.1. Time Variability

In this section, we perform a time resolved analysis of the ionized absorber in NGC 3516. In particular, we identify the parameters that show significant variations among the observations and explore a possible correlation with the changes in flux.

4.1.1. Ionization Parameter U

Phase HI: The most significant change in ionization parameter is given at a level 4σ between observation **8x** and the others. This parameter,

along the nine observations, is plotted in Figure 9 (top plot). We also plot a scaled version of the flux values. This scaled version of the light curve represents the expected changes of U if the gas were instantly in photoionization equilibrium with the ionizing source (for gas in photoionization equilibrium, changes in flux must be followed by changes by the same factor in U). Clearly, this is not observed in the Figure 9, indicating that there is no clear response of this component to the flux variations.

Phase MI: This component presents strong significative changes between observations **1x** and **5x** at 7σ and between observations **5x** to **8x** at 8σ . Interestingly, these changes are correlated with the flux variations. Among observations **1x**, **2x**, **3c** and **4c**, the ionization degree of the phase **MI** changes by nearly the same factor as the X-ray flux. This indicates that this component is responding to the continuum changes close to photoionization equilibrium.

Phase LI: The most important variations in U are found between observations **1x** and **4c** and between observations **2x** and **5x**, both at 4σ . For this phase, there is a reaction to the larger changes in flux in longer timescales, as observed in Figure 9 (bottom panel). From observations **2x** and **4c** the gas presents a delay in recombining as expected in photoionization equilibrium (*PhE*). Yet, at the time of observation **5x**, the gas seems to have found equilibrium again. As the flux increases from observations **5x** to **6c** the gas re-ionizes to reach an ionization state consistent again with *PhE*. Overall, this component also seems to respond, albeit with larger delays and in a more complex way to the changes in the continuum.

Finally, we note that the highest ionization component **VH** (detected only in the hard X-ray band) does not presents significant changes in the ionization parameter. This behaviour is expected because the ionization potential of FeXXV is 8.8 keV and that of FeXXVI is 9.3 keV, and the hard X-rays always vary much less compared to soft X-ray band. Therefore, it is possible that at these relevant energies, the continuum did not vary much. We conclude that the lack of variability cannot be used to use a limit on density for this component.

TABLE 11

COMPARISON BETWEEN THE WARM ABSORBERS FOUND IN TURNER ET AL. 2008, MEHDIPOUR ET AL. 2010 AND THIS WORK .

Model	WA 1	WA 2	WA 3	WA 4
Turner	Zone 1 $\log \xi \sim -0.05$ $N_H \sim 6 \times 10^{21} \text{ cm}^{-2}$ $v_{out} = -200 \text{ kms}^{-1}$	Zone 2 $\log \xi \sim 3$ $N_H \sim 10^{22} \text{ cm}^{-2}$ $v_{out} = -1100 \text{ kms}^{-1}$	Zone 3 $\log \xi \sim 2.5$ $N_H \sim 10^{23} \text{ cm}^{-2}$ $v_{out} = -1100 \text{ kms}^{-1}$	Zone 4 $\log \xi \sim 4.3$ $N_H \sim 10^{23} \text{ cm}^{-2}$ $v_{out} = -1000 \text{ kms}^{-1}$
Mehdipour	Phase A $\log \xi = [0.87-0.97 \pm 0.02]$ $N_H = [0.33-0.43 \pm 0.02] \times 10^{22} \text{ cm}^{-2}$ $v_{out} = -100 \text{ to } -200 \pm 40 \text{ kms}^{-1}$	Phase B $\log \xi = [2.39-2.43 \pm 0.05]$ $N_H = [1.7-3.2 \pm 0.04] \times 10^{22} \text{ cm}^{-2}$ $v_{out} = -1500 \text{ to } -1600 \pm 100 \text{ kms}^{-1}$	Phase C $\log \xi = [2.99-3.07 \pm 0.05]$ $N_H = [1.2-1.7 \pm 0.02] \times 10^{22} \text{ cm}^{-2}$ $v_{out} = -800 \text{ to } -1000 \pm 300 \text{ kms}^{-1}$	
Huerta	Phase LI $\log U = -1.07 \text{ to } -0.54 \pm 0.17$ $N_H = [0.13-0.34 \pm 0.01] \times 10^{22} \text{ cm}^{-2}$ $v_{out} = -2426 \pm 350 \text{ kms}^{-1}$	Phase MI $\log U = [0.16-0.65] pm 0.04$ $N_H = [0.25-0.40 \pm 0.01] \times 10^{22} \text{ cm}^{-2}$ $v_{out} = -605 \pm 350 \text{ kms}^{-1}$	Phase HI $\log U = [1.76-2.45] pm 0.05$ $N_H = [1.66-3.31 \pm 0.01] \times 10^{22} \text{ cm}^{-2}$ $v_{out} = -1847 \pm 350 \text{ kms}^{-1}$	Phase VH $\log U = [3.49-4.14] pm 0.06$ $N_H = [1.51-1.90 \pm 0.01] \times 10^{23} \text{ cm}^{-2}$ $v_{out} = -2650 \pm 350 \text{ kms}^{-1}$

*Ionization parameter $\xi \equiv L/nr^2$ where L is 1-1000 Rydbergh luminosity, n de gas density and r the absorber-source distance.

*Ionization parameter $U \equiv \frac{Q}{4\pi R^2 n_H c}$.

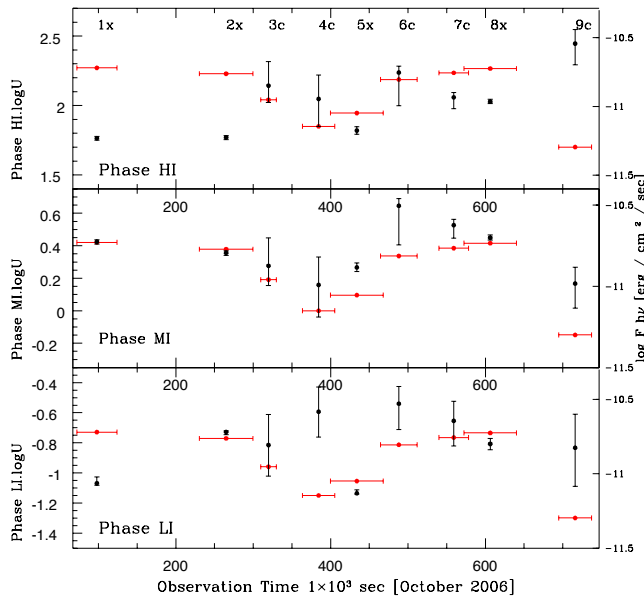


Fig. 9.— In all panels is plotted the light curve of the X-ray [8 - 25 Å] range of NGC 3516 -red-, the flux energy $F_{h\nu}$ was scaled in order to compare it with the logU parameter of each ionized phase. The logU variation in time is plotted for phases **HI** (top panel), **MI** (medium plot) and **LI** (bottom plot).

4.1.2. Equivalent H Column Density

There are mild variations (by a factor $\lesssim 2.5$) in the H equivalent column density along the nine observations, for the three phases detected in the soft X-ray band. The variations are not anti-correlated with the energy flux, as it would be expected in a scenario where the WA consists of material crossing our line of sight, and this material were responsible for producing the flux variation observed in the light curve. Figure 10 shows the changes in this parameter of each ionized phase (phases **HI**, **MI** and **LI**).

In order to study how significant are the changes in column density, we performed a test, fitting all datasets with a single value of N_H . The best fit value for this parameter is similar to the values obtained when modelling individual observations, as expected. However, it is noteworthy that the other parameters are fully consistent with those obtained in Model C. In particular, the values for the ionization parameter are the same, within errors, with those found if N_H is free to vary in each observation. This implies that the variations found in U are not produced or correlated by possible variations in the column density.

4.2. Variations in Spectral Features in the spectra of NGC 3516

Given that the models predict variations in the ionization degree of two ionization phases (**MI** and **LI**), we have studied in detail the spectra of the source to identify clear signatures of such variations.

4.2.1. The Iron M-Shell Unresolved Transition Array

This Fe M-shell *UTA* (Unresolved Transition Array) is extremely useful to look for opacity changes in the absorber phases (as shown by Krokgold et al. (2005)). To look for these changes, we performed a comparison between spectra **1x** and **5x** in the 15 - 18 Å range. Both spectra were normalized using a simple power law to the local continuum. The residuals were over-plotted to search for possible differences. The results are shown in Figure 11. An evident variation in the position of the Fe UTA can be observed between spectra **1x** and **5x** (upper panels in Fig. 11).

In the bottom panel of Figure 11 we present

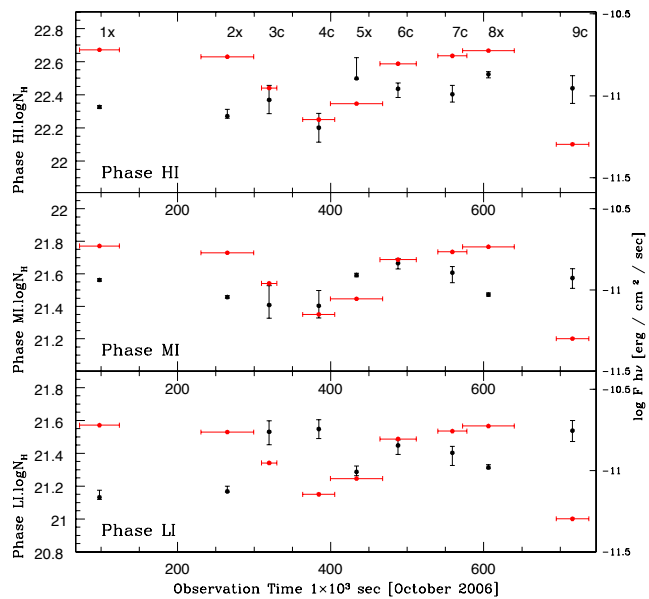


Fig. 10.— The $\log N_H$ variation in time is plotted for phases **HI** (top panel), **MI** (medium plot) and **LI** (bottom plot). The flux energy $F_{h\nu}$ (in red) was scaled in order to compare it with the $\log N_H$ parameter of each ionized phase.

the expected opacity changes in this spectral region, in response to a variation by a factor of ~ 2 in the ionizing flux. This change is similar to the flux variation between observations **1x** and **5x**, so it closely matches an scenario were the gas is in photoionization equilibrium. It is clear that the observed variations are consistent with those expected in photoionization equilibrium for components **MI** and **LI**, that produce the UTA.

Figure 12 compares the Fe M-shell UTA between different Chandra spectra. This plot shows a similar variability trend (although less significant) between observations **4c** and **6c**, again pointing to gas close to photoionization equilibrium. Furthermore, no spectral variations are found between observations **6c** and **7c**, where the flux remains constant.

4.2.2. Testing Possible Changes in Covering Factor

The observed changes in column density (although not very drastic) could be produced by real changes in the total column towards the source or by possible variations in the covering factor of partial covering absorbers. To further investigate this, and to explore if the changes in flux might be connected with changes in covering factor (as suggested by Turner et al. (2008)), we have also looked at the two extreme XMM-Newton flux states (**1x** and **5x**). We used two intense Oxygen absorption lines, OVIII- $K\alpha$ and OVII- $K\beta$ to track these possible changes. As seen in Figure 8, these two lines track absorption by the three components found in the soft X-ray band. Given that these lines are saturated, their maximum depth should depend mainly in the fraction of the source covered by the absorber (*i.e.* the residual observed emission should give us directly the part of the source not covered). Therefore, changes in covering factor should produce variations in the depth of these lines. This is clearly shown in Figure 13 (upper left panel) where we present a model assuming a change in the covering factor from 40% to 70% (as reported in Turner et al. (2008)). In Figure 13 (upper right and bottom panels) we present the normalized data for spectra **1x** and **5x**, and **7c**, and **9c**. It is clear that the absorption lines do not change significantly between these states, the variations are within the error bars. Any possible variations does not follow the expected direction

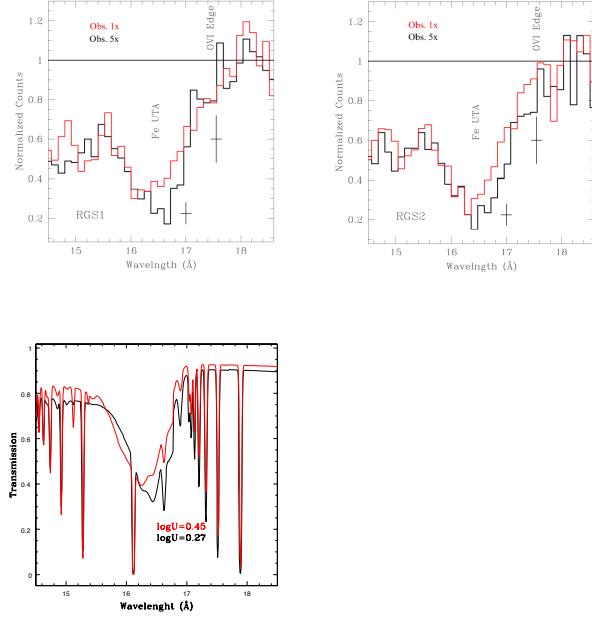


Fig. 11.— Fe M-shell UTA comparison between **1x** and **5x** spectra of RGS from XMM-Newton. For RGS 1 top panel left and for RGS 2 top panel right [14.5 - 18.5 Å]. In the bottom panel is plotted the opacity variation produced by a change in the ionizing flux by a factor of 2 in photoionization equilibrium (modelled with the *PHASE* code (Krongold et al. 2003)).

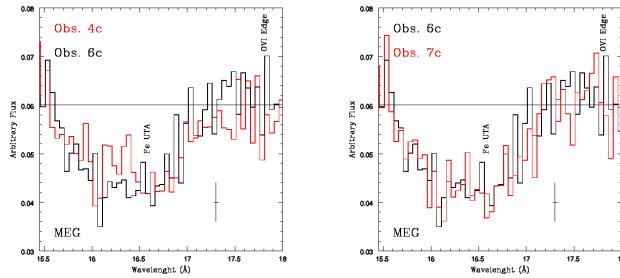


Fig. 12.— Fe M-shell UTA comparison between Chandra data from 15.5 to 18.5 Å range. Left panel: observations **4c** and **6c**. Right panel: observations **6c** and **7c**.

for a change in covering factor responsible for the flux changes. Rather, the data hints to a change where the absorption lines become deeper during the high states, as expected if the gas is responding to the changes in the continuum. The same comparison was performed among the Chandra data with a similar results.

The most striking result is obtained when comparing the NeIX absorption feature between Chandra observations. As it can be observed in Figure 14, there is a significant change in the depth of NeIX transition, between observations **7c** and **9c**. This change can be easily understood as the response in ionization state of the gas in response to impinging flux. Furthermore, the change is exactly the opposite to the one expected if the changes in flux were produced by changes in the covering factor.

Therefore, the high resolution spectra do not support a scenario where the covering factor of the absorber is changing. This result is consistent with those of Mehdipour et al. (2010), who reached the same conclusion using data models. Thus, both data and models suggest that the changes in flux are not due to changes in covering factor of the ionized absorber as suggested by Turner et al. (2008). Rather, our analysis (using models and direct comparison of spectra) indicates that the changes in spectral features are consistent with opacity changes following flux variations.

5. Discussion

5.1. Location and Density of the Ionization Components

The time variability analysis of the ionized absorber can lead us to constrain the number density of the gas and thus break the degeneracy between this quantity and the distance to the continuum source. As shown by Nicastro et al. (1999), the photoionization equilibrium time of a cloud of gas in response to variations in the ionized continuum is inversely proportional to the density of the cloud, according to the following formula:

$$t_{eq}^{x^i, x^{i+1}} \sim \left\{ \frac{1}{\alpha_{rec}(x^i, T_e)_{eq} n_e} \right\} \times \left\{ \frac{1}{[\alpha_{rec}(x^{i-1}, T_e) / \alpha_{rec}(x^i, T_e)]_{eq} + (n_{X^{i+1}} / n_{X^i})} \right\}$$

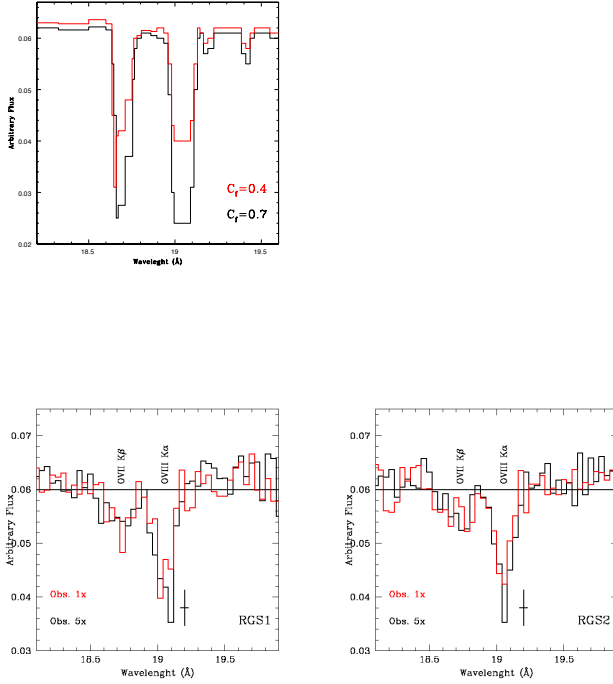


Fig. 13.— OVII-K β and OVIII-K α absorption lines [18 - 20 Å], the first panel (top) is the model assuming that the covering factor is changing. The second (bottom left) and third (bottom right) panels contain the OVII-K β and OVIII-K α absorption lines for observations **1x** and **5x** with the RGS1 and RGS2 from XMM, respectively.

where t_{eq} is the photoionization equilibrium time, T_e is the electron temperature and $\alpha_{rec}(x^i)$ is the radiative recombination rate coefficient (obtained from Shull & van Steenberg (1982)) for the ions x^i and x^{i+1}). We have used the response times detected in §4.1 to constrain in the photoionization equilibrium timescale of the gas, and thus, in the density of the gas.

5.1.1. Phase MI Location

The ionization state of this component follows closely the flux changes. Thus, the photoionization equilibrium timescale must be smaller than the typical elapsed time between observations. Using observations **4c** to **5x**, we find $t_1=15.12$ ksec (t_1 is defined as the time between observations **4c** to **5x**), thus $t_{eq} \lesssim t_1 = 15.12$ ksec.

Using the electronic temperature for this phase ($T_e = 9.8 \times 10^4$ K) and the recombination rates for OVII and OVIII, we find $n_e > 4.9 \times 10^6 \text{ cm}^{-3}$. From the measured value of U^1 and the inferred luminosity of photons of the central engine ($Q \cong 4.0 \times 10^{53}$ photons/s), this implies that the distance of component **MI** to the central source must be $R_{MI} < 3.4 \times 10^{17}$ cm or $R_{MI} < 0.11$ pc. Kraemer et al. (2002) estimated the dust sublimation radius of NGC 3516 as $R_{sub} \lesssim 2.7 \times 10^{17}$ cm, assuming a dust sublimation temperature of 1500 K. Thus, this component is marginally consistent with the dust sublimation radius. However, we note that in the torus wind model of Krolik & Kriss (2001), the outflow must arise far beyond this radius, well into the “obscuring torus”. (see Krongold et al. (2007) for a detailed discussion). Then, we consider more likely that this component arises from the accretion disk as suggested by Netzer et al. (2002).

5.1.2. Phase LI Location

According with the response observed in the ionization degree of the phase **LI**, two different timescales can be estimated. First, during the recombination phase from observations **2x** and **4c** this phase does not reach photoionization equilibrium with the impinging flux (see Figure 9). Therefore, $t_{eq} > 125$ ksec, the time elapsed between these two observations. On the other hand, during the ionization episode between observations **5x** and **6c**, that lasted ~ 50 ksec, this ab-

sorbing component reached photoionization equilibrium with the source. We note that the different photoionization equilibrium timescales presented above are not incompatible with each other. Equilibration times are much larger during recombination phases than ionization ones. With these two constraints, and the electron temperature of this component $T_{e,LI} = 3.0 \times 10^4$ K, we find a density $7.8 \times 10^5 \text{ cm}^{-3} \lesssim n_{e,LI} \lesssim 1.9 \times 10^6 \text{ cm}^{-3}$. This in turn, imply that the distance of this component to the central source should be between $1.8 \times 10^{18} \text{ cm} \lesssim R_{LI} \lesssim 2.9 \times 10^{18} \text{ cm}$. This component is likely arising from the dusty torus, as suggested by Krolik & Kriss (2001). However, we note that the flow might originate close to the region were we are observing it. Thus, a disk wind cannot be strictly ruled out.

5.1.3. Phase HI Location

The location of phase **HI** is more uncertain. The response timescale to the changes in the ionization flux should be greater than the duration of the low flux episode in the entire observation. From Figure 9, the low flux episode lasted ~ 200 ksec from observations **3c** to **6c**. Thus, the density for phase **HI** must be $n_e > 6.4 \times 10^4 \text{ cm}^{-3}$ (using a temperature of $T_{e,HI} = 4.5 \times 10^5$ K and FeXVIII and Fe XIX charge states). Therefore, the minimum distance to the central source for phase **HI** is $R_{HI} \sim 4.0 \times 10^{17} \text{ cm}$, which is around ~ 0.13 pc. The location of this component is consistent with a flow arising in the dusty torus, or a flow arising from the accretion disk, observed further out.

As explained in §4.1.1, the lack of variation in component VH cannot be used to obtain a reliable constrain on distance, given that at higher energies the flux variations are much smaller.

5.2. Does the absorber forms a multi-phase medium?.

It has been suggested by several studies (e.g. Krongold et al. (2003, 2005); Cardaci et al. (2009)) that the structure of ionized absorbers could be that of a multi-phase medium in pressure balance. A multi-phase medium requires absorbers with similar outflow velocities to avoid drag forces to destroy one of the components. Clearly, component **MI** cannot be part of the same

flow as components **LI** and **HI**, as these components are located farther out from the central source and they have a much faster outflow velocity. However, components **LI** and **HI** have a similar outflow velocity and they may be located at a similar distance from the central source. Then, it is possible that this components indeed form a multi-phase medium.

In order to further study this possibility, the thermal equilibrium (S -curve) obtained for the spectral distribution (SED) in this analysis is plotted in Figure 15. This curve presents the points where the gas temperature ($\log T$) and pressure lie in thermal equilibrium. The gas pressure is inversely proportional to the quantity $\log(U/T)$, which can be directly derived in our analysis. Thus, two components can be part of a multi-phase flow if they have different temperatures but similar $\log(U/T)$ values. Assuming solar metallicities (Z_\odot) the S -curve for NGC 3516 (Figure 15) is not multi-valued. Thus, it is not possible that these two components exist in pressure equilibrium.

However, the shape of the S -curve results very sensitive to external heating and cooling sources. Additional cooling can be produced by material with metallicities higher than the solar. In fact, in AGN, supra-solar metallicities are expected (e.g. Mihalzski & Ferland (1983) & Fields et al. (2007)). A higher amount of cooling material creates an S -curve more vertical and together a possible “multi-phase” system. With the goal to explore this possibility we present a model with 5 times solar metallicity ($5Z_\odot$). Figure 16 shows that if the metallicity of the WA is higher than solar, then components **LI** and **HI**, could coexist in pressure equilibrium given that the pressure of both absorbers are in the same order of magnitude. As seen in the plot, for a metallicity $5Z_\odot$, the difference between the gas pressure of these components is not significative.

5.3. Intrinsic Variability vs. Obscuration Scenarios for the Flux changes in NGC 3516

Two possible scenarios have been suggested to explain the observed variability in the X-ray emission of NGC 3516. The first one suggests intrinsic variations of the central source (Mehdipour et al. 2010). In the second scenario, explored by Turner

et al. (2008) and Markowitz et al. (2008), they proposed that the variations are due to obscuration of the central source produced by near blobs of material, either ionized or neutral. In particular Turner et al. (2008) suggest that an absorbing component of ionized material (their "heavy absorber") presents a change in the covering factor, that is responsible for the observed flux variations. Such component would produce absorption by ions of OVIII and OVII (Turner et al. 2008). However, we could not find evidence of covering factor variations in the OVII-K β and OVIII-K α lines (Figure 13).

To further explored this possibility, we fit the spectra using a partial covering absorber. We note that partial covering is not required by the data, as a fit including it does not improve over a fit with fully covering absorbers (in agreement with Mehdipour et al. (2010)). Nevertheless, based on **Model C** a partial covering was tested in all the possible combinations, including this factor in one, two and the three ionizing components, that imprint spectral features in the soft X-ray band.

The best solution found included partial covering in phase **HI**. However, the value of the covering factor is almost unity in all observations (see Table 12), and does not anti-correlate with the flux. An F-test indicates that varying the covering factor is not needed (confidence of 57% if we compare the model which does not include the covering factor and this model). Thus, our results do not support a scenario in which the covering factor of the warm absorbers is responsible for the flux variations. If these variation are indeed produced by obscuring material, this material should be located closer in than the warm absorbing components, as components **LI** and **MI** are responding to the observed flux variations.

6. Conclusions

We summarize our results as follows:

1. We modelled the nine X-ray 2006 data of XMM-Newton and Chandra. The best statistical model consists of a complex and variable continuum emission component, and also includes nine emission lines of different ionized species in the soft X-ray band. An additional emission line is required in the X-ray hard band, where the Fe-K α emission line is present. The continuum emission

is absorbed by four different ionized phases (warm absorbers): three of them produce features in the soft X-ray band and the fourth, with the highest ionization degree, only generates the Fe-K α absorber complex detected in the 6.7 - 7 keV range.

2. The ionization state of the two components with the lowest ionization degree (phases **MI** and **LI**) is responding to the changes in the ionizing continuum. The other two absorbing components (phases **VH** and **HI**) do not seem to react to the ionizing continuum variations.

3. The observed variations in the Fe M-shell UTA (produced by phases **MI** and **LI**) between observations **1x** and **5x** were found to be similar to what is expected for ionized material close to photoionization equilibrium.

4. The response timescale of the phases **MI** and **LI** allow us to constrain their location: for phase **MI** the location is $R_{MI} < 2.7 \times 10^{17}$ cm. For component **LI**, the location must be within the range 1.8×10^{18} cm $\lesssim R_{MI} \lesssim 2.9 \times 10^{18}$ cm. For component **HI**, a lower limit to the location was derived: $R_{HI} \gtrsim 4.0 \times 10^{17}$ cm. The lack of variations in component **VH** cannot be used to find a reliable constraint on its location (see §4.1.1).

5. There is no evidence of a depth change in the main absorber transitions (OVII-K β , OVIII-K α and Ne IX), as expected in a scenario where the covering factor is varying in the time.

6. Finally, if a solar metallicity is assumed (Z_{\odot}), the absorbing components cannot be in pressure equilibrium. However, with higher metallicity values ($5Z_{\odot}$) the *S*-curve becomes more vertical and then, it becomes possible that the absorbers **HI** and **LI** form a multi-phase medium.

We thank the referee for her/his thoughtful and constructive comments that helped to improve the paper. We also thank Doron Chelouche, Maria Santos-Lleo and Ehur Behar for their invaluable help and constructive comments. This research is based on observations obtained with XMM-Newton, an ESA science mission with instruments and contributions directly funded by ESA Member States, and Chandra Space Telescope of NASA.

REFERENCES

Andrade-Velázquez, M., Krongold, Y., Elvis, M., Nicastro, F., Brickhouse, N., Binette, L.,

TABLE 12

COVERING FACTOR VALUES. THE PERCENTAGE OF THE COVERING FACTOR PRESENTS A TYPICAL ERROR OF 5% .

Obs.	1x	2x	3c	4c	5x	6c	7c	8x	9c
Covering Factor %	96%	89%	84%	100%	100%	93%	88%	99%	93%

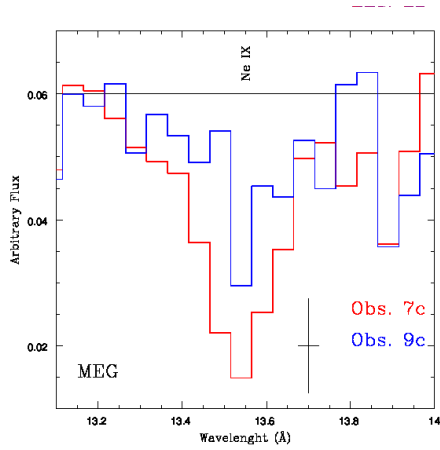


Fig. 14.— Ne IX absorption line compared between Chandra observations **7c** and **9c** in [13, 14 Å] range.

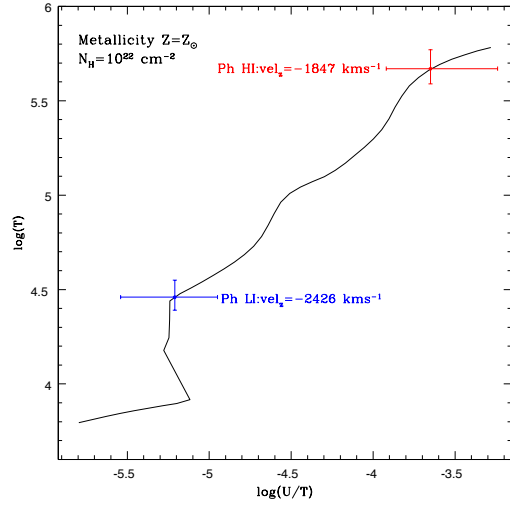


Fig. 15.— Thermal stability curve S of NGC 3516 SED supposing $\log N_H = 10^{22} \text{ cm}^{-2}$ and a solar metallicity Z_\odot . Over-plotted there are the ionized absorbers **HI** and **LI**.

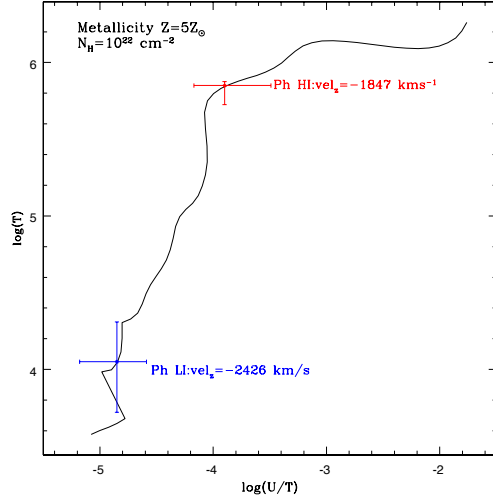


Fig. 16.— Thermal stability S -curve of NGC 3516 SED supposing $\log N_H = 10^{22} \text{ cm}^{-2}$ and supra-solar metallicity $5Z_\odot$. Over-plotted there are the ionized absorbers **HI** and **LI**.

- Mathur, S., & Jiménez-Bailón, E. 2010, *ApJ*, 711, 888
- Arav, N. 2004, *AGN Physics with the Sloan Digital Sky Survey*, 311, 213
- Behar, E., Sako, M., & Kahn, S. M. 2001, *ApJ*, 563, 497
- Blustin, A. J., Page, M. J., Fuerst, S. V., Branduardi-Raymont, G., & Ashton, C. E. 2005, *A&A*, 431, 111
- Canizares, C. R., et al. 2000, *ApJ*, 539, L41
- Cardaci, M. V., Santos-Lleó, M., Krongold, Y., et al. 2009, *A&A*, 505, 541
- Costantini, E., et al. 2000, *ApJ*, 544, 283
- Crenshaw, D. M., Maran, S. P., & Mushotzky, R. F. 1998, *ApJ*, 496, 797
- Crenshaw, D. M., Kraemer, S. B., & George, I. M. 2003, *ARA&A*, 41, 117
- Di Matteo, T., Springel, V., & Hernquist, L. 2005, *Nature*, 433, 604
- Dickey, J. M., & Lockman, F. J. 1990, *ARA&A*, 28, 215
- Edelson, R., & Nandra, K. 1999, *ApJ*, 514, 682
- Edelson, R., et al. 2000, *ApJ*, 534, 180
- Elvis, M. 2000, *ApJ*, 545, 63
- Ferland, G. J. 1991, *The Ohio State University Internal Report*, 565 pages,
- Fields, D. L., Mathur, S., Krongold, Y., Williams, R., & Nicastro, F. 2007, *ApJ*, 666, 828
- Freeman, P., Doe, S., & Siemiginowska, A. 2001, *Proc. SPIE*, 4477, 76
- Fruscione, A., et al. 2006, *Proc. SPIE*, 6270
- Gabriel, C., et al. 2004, *Astronomical Data Analysis Software and Systems (ADASS) XIII*, 314, 759
- George, I. M., Turner, T. J., Netzer, H., Nandra, K., Mushotzky, R. F., & Yaqoob, T. 1998, *ApJS*, 114, 73
- George, I. M., et al. 2002, *ApJ*, 571, 265

- Goad, M. R., Koratkar, A. P., Kim-Quijano, J., Korista, K. T., O'Brien, P. T., & Axon, D. J. 1999, *ApJ*, 524, 707
- Guainazzi, M., Marshall, W., & Parmar, A. N. 2001, *MNRAS*, 323, 75
- Halpern, J. P. 1984, *ApJ*, 281, 90
- Holczer, T., & Behar, E. 2012, *ApJ*, 747, 71
- Hopkins, P. F., Somerville, R. S., Hernquist, L., et al. 2006, *ApJ*, 652, 864
- Iwasawa, K., Miniutti, G., & Fabian, A. C. 2004, *MNRAS*, 355, 1073
- Jansen, F., et al. 2001, *A&A*, 365, L1
- Keel, W. C. 1996, *AJ*, 111, 696
- Kolman, M., Halpern, J. P., Martin, C., Awaki, H., & Koyama, K. 1993, *ApJ*, 403, 592
- Koratkar, A., et al. 1996, *ApJ*, 470, 378
- Kraemer, S. B., Crenshaw, D. M., George, I. M., Netzer, H., Turner, T. J., & Gabel, J. R. 2002, *ApJ*, 577, 98
- Kriss, G. A., Espey, B. R., Krolik, J. H., Tsvetanov, Z., Zheng, W., & Davidsen, A. F. 1996, *ApJ*, 467, 622
- Kriss, G. A., et al. 1996, *ApJ*, 467, 629
- Krolik, J. H., & Kriss, G. A. 1995, *ApJ*, 447, 512
- Krolik, J. H., & Kriss, G. A. 2001, *ApJ*, 561, 684
- Krongold, Y., Nicastro, F., Brickhouse, N. S., Elvis, M., Liedahl, D. A., & Mathur, S. 2003, *ApJ*, 597, 832
- Krongold, Y., Nicastro, F., Elvis, M., et al. 2005, *ApJ*, 620, 165
- Krongold, Y., Nicastro, F., Brickhouse, N. S., Elvis, M., & Mathur, S. 2005, *ApJ*, 622, 842
- Krongold, Y., Nicastro, F., Elvis, M., Brickhouse, N., Binette, L., Mathur, S., & Jiménez-Bailón, E. 2007, *ApJ*, 659, 1022
- Krongold, Y., Elvis, M., Andrade-Velazquez, M., et al. 2010, *ApJ*, 710, 360
- Longinotti, A. L., et al. 2010, *A&A*, 510, A92
- Longinotti, A. L., Krongold, Y., Kriss, G. A., et al. 2013, *ApJ*, 766, 104
- Maccacaro, T., Garilli, B., & Mereghetti, S. 1987, *AJ*, 93, 1484
- Maoz, D., Markowitz, A., Edelson, R., & Nandra, K. 2002, *AJ*, 124, 1988
- Markowitz, A., & Edelson, R. 2004, *ApJ*, 617, 939
- Markowitz, A., et al. 2006, *Astronomische Nachrichten*, 327, 1087
- Markowitz, A., et al. 2008, *PASJ*, 60, 277
- Mathur, S., Elvis, M., & Wilkes, B. 1995, *ApJ*, 452, 230
- Mathur, S., Wilkes, B. J., & Aldcroft, T. 1997, *ApJ*, 478, 182
- McKernan, B., Yaqoob, T., & Reynolds, C. S. 2007, *MNRAS*, 379, 1359
- Mehdipour, M., Branduardi-Raymont, G., & Page, M. J. 2010, *A&A*, 514, A100
- Mihalszki, J. S., & Ferland, G. J. 1983, *MNRAS*, 205, 1279
- Morse, J. A., Wilson, A. S., Elvis, M., & Weaver, K. A. 1995, *ApJ*, 439, 121
- Nandra, K., & Pounds, K. A. 1994, *MNRAS*, 268, 405
- Nandra, K., George, I. M., Mushotzky, R. F., Turner, T. J., & Yaqoob, T. 1999, *ApJ*, 523, L17
- Netzer, H., Chelouche, D., George, I. M., Turner, T. J., Crenshaw, D. M., Kraemer, S. B., & Nandra, K. 2002, *ApJ*, 571, 256
- Netzer, H., et al. 2003, *ApJ*, 599, 933
- Nicastro, F., Fiore, F., Perola, G. C., & Elvis, M. 1999, *ApJ*, 512, 184
- Piconcelli, E., Jimenez-Bailón, E., Guainazzi, M., Schartel, N., Rodríguez-Pascual, P. M., & Santos-Lleó, M. 2004, *MNRAS*, 351, 161
- Piconcelli, E., Jimenez-Bailón, E., Guainazzi, M., Schartel, N., Rodríguez-Pascual, P. M., & Santos-Lleó, M. 2005, *A&A*, 432, 15

- Reynolds, C. S., Fabian, A. C., Nandra, K., Inoue, H., Kunieda, H., & Iwasawa, K. 1995, *MNRAS*, 277, 901
- Reynolds, C. S. 1997, *MNRAS*, 286, 513
- Ricci, C., Beckmann, V., Audard, M., & Courvoisier, T. J.-L. 2010, *A&A*, 518, A47
- Róžańska, A., Goosmann, R., Dumont, A.-M., & Czerny, B. 2006, *A&A*, 452, 1
- Shull, J. M., & van Steenberg, M. 1982, *ApJS*, 48, 95
- Smith, R. K., Brickhouse, N. S., Liedahl, D. A., & Raymond, J. C. 2001, *ApJ*, 556, L91
- Turner, T. J., Kraemer, S. B., George, I. M., Reeves, J. N., & Bottorff, M. C. 2005, *ApJ*, 618, 155
- Turner, T. J., Reeves, J. N., Kraemer, S. B., & Miller, L. 2008, *A&A*, 483, 161
- Turner, T. J., Miller, L., Kraemer, S. B., & Reeves, J. N. 2011, *ApJ*, 733, 48
- Véron-Cetty, M.-P., & Véron, P. 2006, *A&A*, 455, 773
- Voit, G. M., Shull, J. M., & Begelman, M. C. 1987, *ApJ*, 316, 573
- Walter, R., Courvoisier, T. J.-L., Ulrich, M.-H., & Buson, L. M. 1990, *A&A*, 233, 53
- Weisskopf, M. C., Tananbaum, H. D., Van Speybroeck, L. P., & O'Dell, S. L. 2000, *Proc. SPIE*, 4012, 2
- Yaqoob, T., & Padmanabhan, U. 2004, *ApJ*, 604, 63